Enhanced, Live-Cell, Super-Resolution Imaging and Single-Molecule Emission Spectrum Reshaping
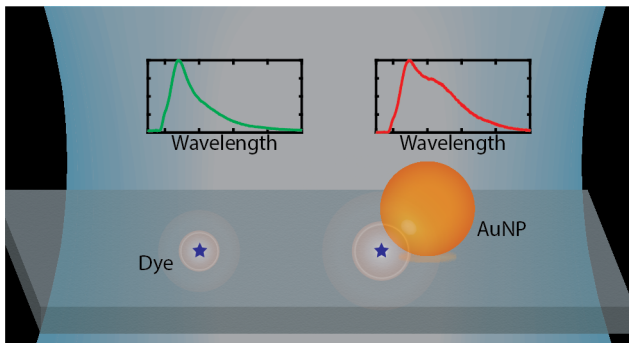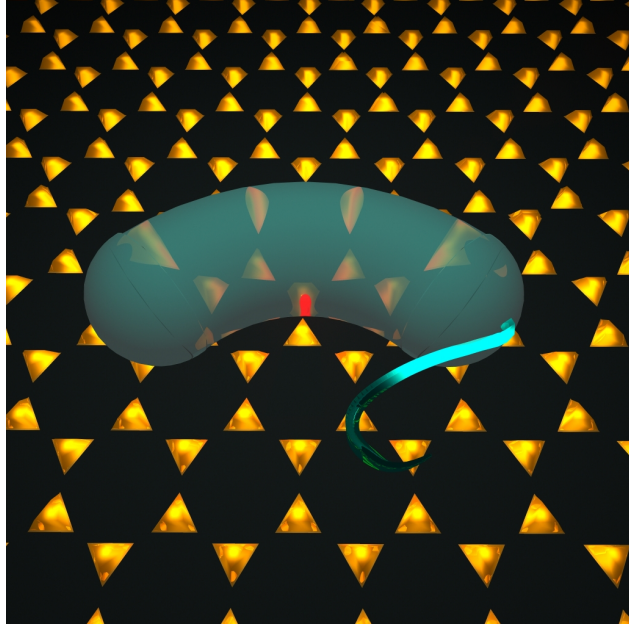
by

Stephen Lee

A dissertation submitted in partial fulfillment
of the requirements for the degree of
Doctor of Philosophy
(Chemistry)
in The University of Michigan
2019

Doctoral Committee:

      Associate Professor Julie S. Biteen, Chair
      Assistant Professor Andy Ault
      Professor Zhan Chen
      Assistant Professor Somin Eunice Lee

Wavelength Wavelength

Dye AuNP

Stephen Lee

stevalee@umich.edu

ORCID iD: 0000-0003-2614-286X

For Ardelia, Ellowyn & Kira

For their steadfast presence and encouragement.

ACKNOWLEDGEMENTS

TABLE OF CONTENTS

LIST OF FIGURES

Figure

LIST OF TABLES

Table

LIST OF ABBREVIATIONS

AuNP gold nanoparticle

DFS dark-field spectroscopy

EBL electron-beam lithography

EMCCD electron multiplying charge-coupled device

FDTD finite difference time domain

LDOS local density of (photonic) states

LSPR localized surface plasmon resonance

NA numerical aperture

NP nanoparticle

NPA nanoparticle array

NSL nanosphere lithography

NT nanotriangle

NTA nanotriangle array

PAINT points accumulation for imaging in nanoscale topography

PALM photoactivated localization microscopy

PSF point spread function

SEM scanning electron microscope

ABSTRACT

Live-cell imaging elucidates subcellular dynamics, and single-molecule imaging extends the capabilities of fluorescence microscopy to the scale of tens of nanometers. To understand the physics of cellular processes on the molecular scale, accurate and precise localization of single molecules is important. The molecule localization precision is related to the brightness of the fluorescence emission, which is sensitive to the local environment. Plasmonic nanoparticles, which act as optical antennas, can enhance the brightness of nearby fluorophores for improved live-cell super-resolution imaging. Additionally, single-molecule fluorescence imaging makes it possible to study light-matter interactions, such as plasmon-enhanced fluorescence, on the nanometer scale. The enhancement of fluorophores is through both a redistribution in the excitation field and a change in the radiative and nonradiative pathways.

In this Thesis, I investigate the effect of the properties of gold nanoparticle arrays, such as particle size, shape and array pitch, on the enhancement factors for plasmon-enhanced live-cell super-resolution imaging, I study the spectral effects of single dyes coupled to individual plasmonic nanoparticles, and I work toward developing an all-fluorescence method for nanothermometry. Chapter I details the background of single-molecule super-resolution fluorescence imaging, plasmon-enhanced fluorescence, and nano-fabrication of plasmonic substrates for fluorescence imaging.

To investigate the live-cell enhancement factors, in Chapter II, I use photoactivation localization microscopy to measure the intensities of single fluorescent proteins in live cells that are imaged on nanosphere lithographed gold nanotriangle arrays of different sizes

and pitches. The results of this work demonstrate how fluorescence enhancement depends on the array characteristics and indicate the ability of plasmonic nanoparticle arrays to increase the brightness of a fluorescent protein in living bacteria. The use of plasmonic substrates for enhanced live-cell imaging is generally accessible for membrane-associated targets, and nanosphere lithography is a cheap and easy method for making the plasmonic substrates.

Although we were able to enhance the fluorescence in living cells, we propose to improve the enhancement beyond two-fold by examining a wider range of nanoparticle sizes, nanoparticle shapes, array order, and array pitch. In Chapter II, I present the use of electron-beam lithography to fabricate a wide range of nanoparticle arrays and I measure their optical responses. I use dark-field scattering spectroscopy to measure the resonance strength and spectrum of the nanoparticle arrays, building on conclusions from earlier in Chapter II. Electron-beam lithography allows for tighter control over the particles and arrays for more carefully tuned substrates for enhanced live-cell imaging.

In addition to live-cell enhancement, single-molecule super-resolution imaging enables studies of light-matter interactions. Plasmon-enhanced fluorescence is a distance- and wavelength-dependent process, and super-resolution hyperspectral imaging allows us to study the heterogeneity of coupling. In Chapter III, I study the distance and spectral dependencies of enhanced fluorescence by combining super-resolution imaging with hyperspectral imaging for simultaneous super-localization and spectroscopy. These results demonstrate the power of single-molecule hyperspectral imaging to elucidate subtle changes in the emission spectrum upon plasmon-coupled fluorescence.

In Chapter IV, I present relevant future directions for super-resolution imaging and studies of light-matter interaction such as: single-particle photoluminescence imaging to study the power and temperature dependence of gold nanoparticle photoluminescence, integrating plasmonics and microfluidics for active control of cellular environments with enhanced imaging, and hyperspectral polarization imaging for information dense imaging

of many fluorophores in complex environments.

CHAPTER I

Introduction

1.1 Optical Microscopy

Optical microscopy has been a critical technique in all fields of science for centuries [1]. Although the first microscopes were simple, single lens instruments, they were capable of magnifications of over 100×, allowing early scientists, then known as natural philosophers, to discover and characterize the microscopic world. Although microscopes have undergone immense improvements over the centuries, such as eliminating aberrations and increasing magnification, one basic limitation of optical microscopes remains: the diffraction limit [2]. The ultimate limitation in microscope resolution is the wave-particle duality that is exhibited by all particles: the wave nature of photons leads to the diffraction limit (Equation 1.1). For example, 400 nm light collected with a 1.4 NA objective would have a diffraction limit of $d = 143$ nm.

$$d = \frac{\lambda}{2NA} \tag{1.1}$$

where λ is the wavelength of emitted light and the numerical aperture (NA) is defined as $NA = n \sin \theta$ where n is refractive index, and θ is the collection angle of the objective.

One simple solution to overcome the optical wavelength diffraction limit is to use some other means of "illumination" that has a smaller wavelength and thus a smaller diffraction limit. Electron microscopy, which uses high-energy electrons to interact with a substrate,

surpasses the optical wavelength diffraction limit to a sub-nanometer scale. This resolution gain is at the expense of having to perform the microscopy in high vacuum on fixed samples with potential damage from the high energy electrons, though advances in sample preparation and *in situ* methods are obviating these concerns [3]. While the limitations of electron microscopy presented here may be of little or no concern for some applications, they mostly preclude the use of electron microscopy for live-cell analyses where subcellular and intercellular dynamics are studied. Thus, in spite of optical microscopy having a relatively large diffraction limit, it is incredibly important for cellular analyses and the study of how light interacts with materials, both of which are focuses for this body of research. I will note that electron microscopy can inform us about some light-matter interactions, although indirectly [4]. Additionally, optical and biochemical techniques can be employed to improve the specificity and contrast of optical microscopy. Two such techniques relevant to this work are fluorescence and dark-field microscopies.

1.1.1 Fluorescence microscopy and super-resolution imaging

Fluorescence, the absorption of a photon and subsequent emission of a photon of lower energy (Figure 1.1a), is utilized in optical microscopy to greatly enhance the contrast and specificity of the objects imaged. In fluorescence microscopy, a sample is labeled with fluorescent probes, which are selected for based on their excitation and emission spectra and their structural target. The sample is then imaged under monochromatic illumination and the emitted light is collected. An example diagram of an epi-fluorescence microscope setup is depicted in Figure 1.1b. Here, a laser is used to excite the fluorophores with wide-field illumination by focusing the beam on the back focal plane of the objective using an imaging lens and dichroic filter. In an "epi" setup, the same objective used for illumination collects the scattered light and emission from the fluorophores. The elastically scattered light is filtered by the dichroic and long-pass filters, while the fluorescence or longer wavelength inelastically scattered light is transmitted and focused onto the camera, in
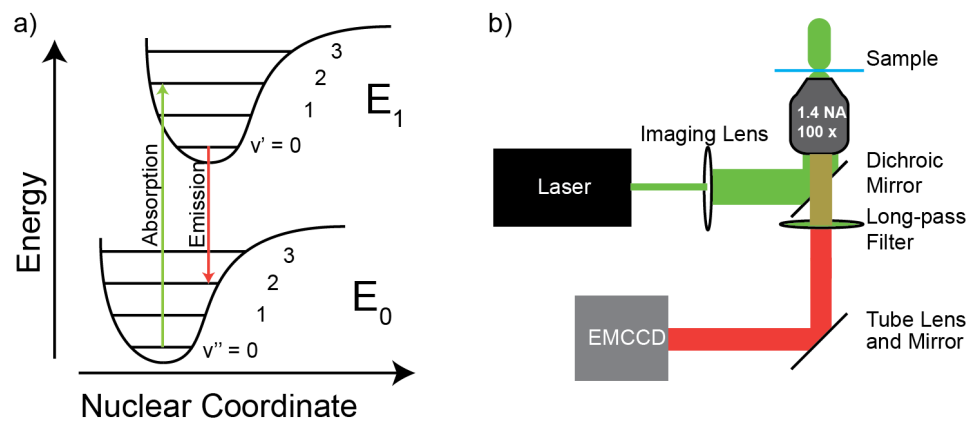
Figure 1.1: Fluorescence energy diagram and fluorescence microscope diagram. (a) Fluorescence energy diagram illustrating the absorption of a green photon and emission of a red photon. (b) A simple fluorescence microscope with monochromatic laser excitation and an electron multiplying charge coupled device detector.

this case an electron multiplying charge-coupled device (EMCCD) detector. The image contrast and specificity are improved over transmission microscopy by filtering out the illumination light and collecting only the light emitted from the fluorescent probes. Thus, objects of interest appear as bright features with a dark background that can be selectively imaged based on excitation or emission wavelength. As technology and methodology progressed and more sensitive cameras were developed, single molecules were eventually able to be detected then imaged [5–7]. The image of a single fluorophore appears as a diffraction-limited spot with point spread function (PSF) defined by an Airy disk (Equation 1.2);

$$I(\theta) = I_0 \left(\frac{2J_1(x)}{x} \right)^2 \tag{1.2}$$

where I_0 is the maximum intensity of the Airy disk center, J_1 is is the first order Bessel function of the first kind and $x \approx \frac{\pi r}{d}$ where r is the radial distance from the center of the optical axis in the focal plane and d is the diffraction limit defined in Equation 1.1. For the diffraction limited signal produced by a single emitter, we assume that the center of the intensity distribution under normal imaging conditions, i.e. no PSF engineering, is the actual location of the emitter, thus breaking the diffraction limit (Figure 1.2) [8–10].

We can extend this super-localization of a single molecule to super-resolution microscopy by determining the super-localized positions of many single molecules from a diffraction-limited image or image sequence. The super-resolution techniques that fall within this description and are used within this thesis are: points accumulation for imaging in nanoscale topography (PAINT) and photoactivated localization microscopy (PALM) [11, 12]. The PAINT technique relies on having fluorophores in a solution stochastically adsorb and desorb from the structure of interest such that only one fluorophore is emitting within a diffraction-limited spot at a time and the solvated fluorophores cannot be imaged. The PALM technique on the other hand utilizes a photoactivatable fluorophore. A sparse subset of the photoactivatable fluorophore is converted from a non-emissive to an emissive state with a low-power activation pulse. The emissive fluorophore can then be
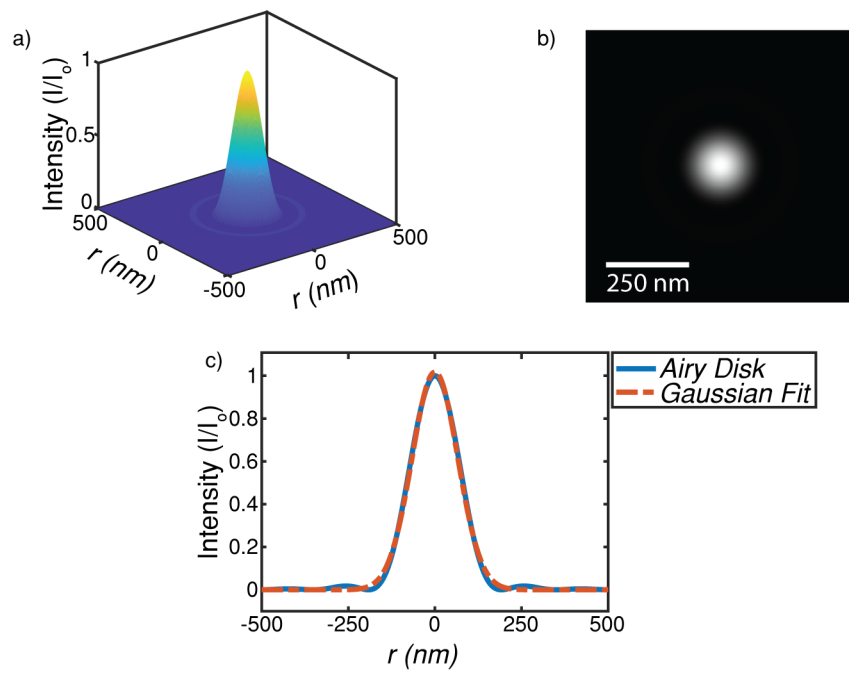
Figure 1.2: PSF and Gaussian fitting. (a) 3D view of an Airy disk PSF with the same parameters in the example for Equation 1.1. (b) Grey scale image of (a) as seen on a camera. (c) Gaussian fit to cross section of (b).

super-localized until it returns to the non-emissive state or irreversibly bleaches, at which point a subsequent activation pulse can repeat the sequence. Regardless of which technique is used, once the single-molecule criterion is met, the fluorophore can be super-localized and the characteristics of the fluorophore can be studied or a super-resolution image can be constructed.

1.1.2 Dark-field microscopy

The second method I present for improving the contrast of optical microscopy is dark-field microscopy. A dark-field microscope illuminates the sample with incident light at an angle that is blocked out on the detection side, and any light that is scattered by the sample and has a different angle than the incident light is collected (Figure 1.3). The object imaged on a dark-field microscope appears bright against a dark background. This method is especially useful for objects with high scattering cross sections, since the object will appear brighter the more it scatters. If the scattered light is originating from a single object, the geometric center of the object can be determined using the same principles of super-localization in fluorescence imaging. Thus, the position of a sub-diffraction limited object can be determined with high accuracy.

1.2 Plasmon-Enhanced Fluorescence

1.2.1 Plasmonics

Metal nanoparticles have been rapidly growing in popularity as a the potential applications for their use have dramatically expanded, such as for enhanced spectroscopy, catalysis, light concentration, and photothermal conversion [13–16]. The primary phenomenon that makes metal nanoparticles useful is the localized surface plasmon resonance (LSPR). This confined, collective oscillation of conduction band electrons (Figure 1.4), acts as a nano-optical antenna by converting free-space light into local electromagnetic energy and *vice*
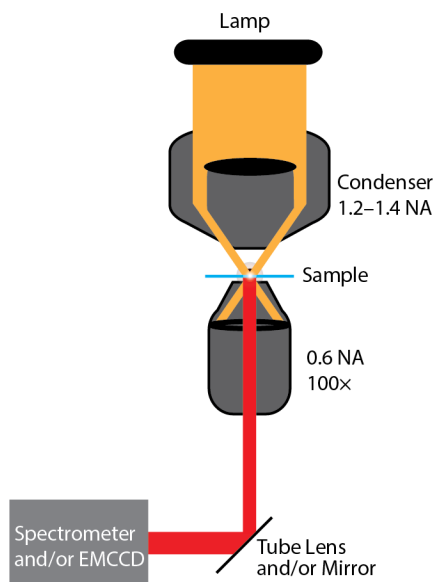
Figure 1.3: Dark-field microscope diagram. Light from a lamp (yellow) is collected by a condenser to form an annular illumination field which is focused on the sample. A low NA objective collects the scattered and blocks the transmitted light. The collected scattered light (red) either is focused on a camera for imaging or dispersed through a spectrometer.
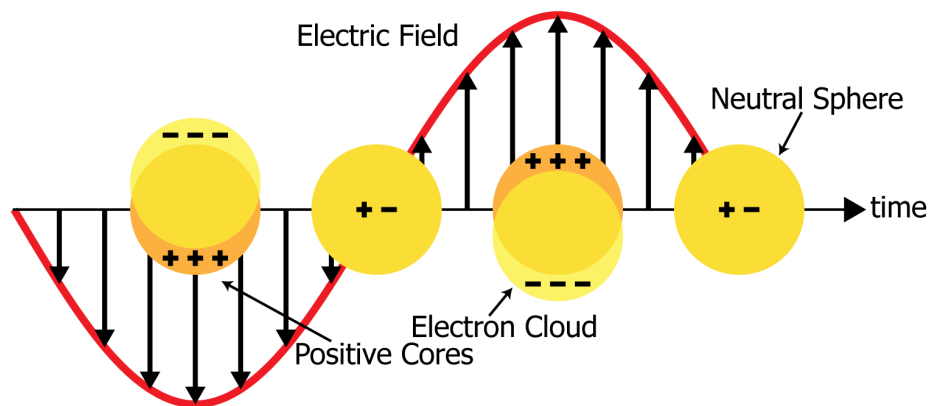
Figure 1.4: Light-induced LSPR. Induced oscillation of conduction band electrons in a sub-wavelength sized sphere. Adapted from [20].

versa [17]. The LSPR depends on the properties of the metal nanoparticle; such as material, size, shape, and surrounding medium [18–21]. One of the most common plasmonic nanoparticle materials is gold, which is popular due to its low reactivity, tunable LSPR throughout the visible and infrared spectrum, and relatively high plasmonicity—how well a substance can support a plasmon—second only to silver in the visible region [22, 23].

1.2.2   Plasmon-enhanced fluorescence

The localization precision of a super-localized fluorophore, defined as the mean squared error in position, $\langle (\Delta x)^2 \rangle$, that can be achieved through PSF fitting is arbitrary high and depends upon only a few parameters [24]:

$$\langle (\Delta x)^2 \rangle = \frac{s^2 + a^2/12}{N} + \frac{4\sqrt{\pi}s^3 b^2}{aN^2} \tag{1.3}$$

where s is the standard deviation of the PSF, a is the pixel size, N is the number of photons collected, and b is the background noise. The readily adjustable parameter in Equation 1.3 that does not require changing the microscope equipment is the total number of detected photons from the fluorophore, N. Fluorophore brightness can be controlled by increasing the extinction coefficient or the quantum yield via novel dye synthesis or fluorescent protein engineering. Alternatively, the optical properties of a fluorophore can be changed by augmenting the local dielectric constant around the fluorophore by changing the media or by engineering the local density of (photonic) states (LDOS), for instance by positioning the dye molecule in the near field of a gold nanoparticle (AuNP). A AuNP can improve the photon yield of a fluorophore by increasing either the excitation field intensity or the radiative rate of the fluorophore [25–28]. A fluorophore in close proximity to a AuNP that is resonantly excited can experience much higher excitation fields than in homogeneous medium. Additionally, a fluorophore can drive a LSPR, which can increase the far-field radiation of the fluorophore, by increasing the LDOS. Thus, the localization precision of

a fluorophore can be immensely improved by carefully selecting an appropriate AuNP antenna for a given fluorophore.

Plasmonic nanoparticles are not only useful in improving the optical properties of fluorophores for super-resolution microscopy, they are also interesting in themselves. Super-resolution microscopy is a powerful tool for unveiling the properties and mechanisms of plasmons and plasmon-enhanced fluorescence. Properties such as the distance, shape, and size dependence of enhancement and the mechanisms of emission polarization, PSF, and spectrum reshaping are uniquely accessible through super-resolution methods [28–33].

1.3 Nanolithography

It is important to understand the substrate fabrication process so that the advantages and limitations of the fabrication process can be considered when making a substrate. There are two major classes of lithography for making the plasmonic nanoparticle substrate: top-down and bottom-up. Here, I will discuss the strengths and weaknesses of each as well as different methods within these classes through the lens of fabricating a sample for epi-fluorescence, single-molecule microscopy.

1.3.1 Methods used in this thesis

In this thesis, I use three methods for fabricating plasmonic substrates: nanosphere lithography (NSL) and electron-beam lithography (EBL) Chapter II and drop-castingin Chapter III and IV. NSL involves the bottom-up assembly of microspheres into a hexago-nally packed monolayer, which is used as a deposition mask to form gold nano-triangles after the nanospheres are removed, (Figure 1.5b). EBL is used for increasing the param-eter space over NSL for fabricating gold nanoparticle arrays by adjusting the nanopar-ticle shape, size, and array pitch (Figure 1.5a). Drop-casting was used in conjunction with photolithographed labeled grids to fabricate samples for the spectral reshaping and temperature-dependent photoluminescence experiments (Figure 1.5c).
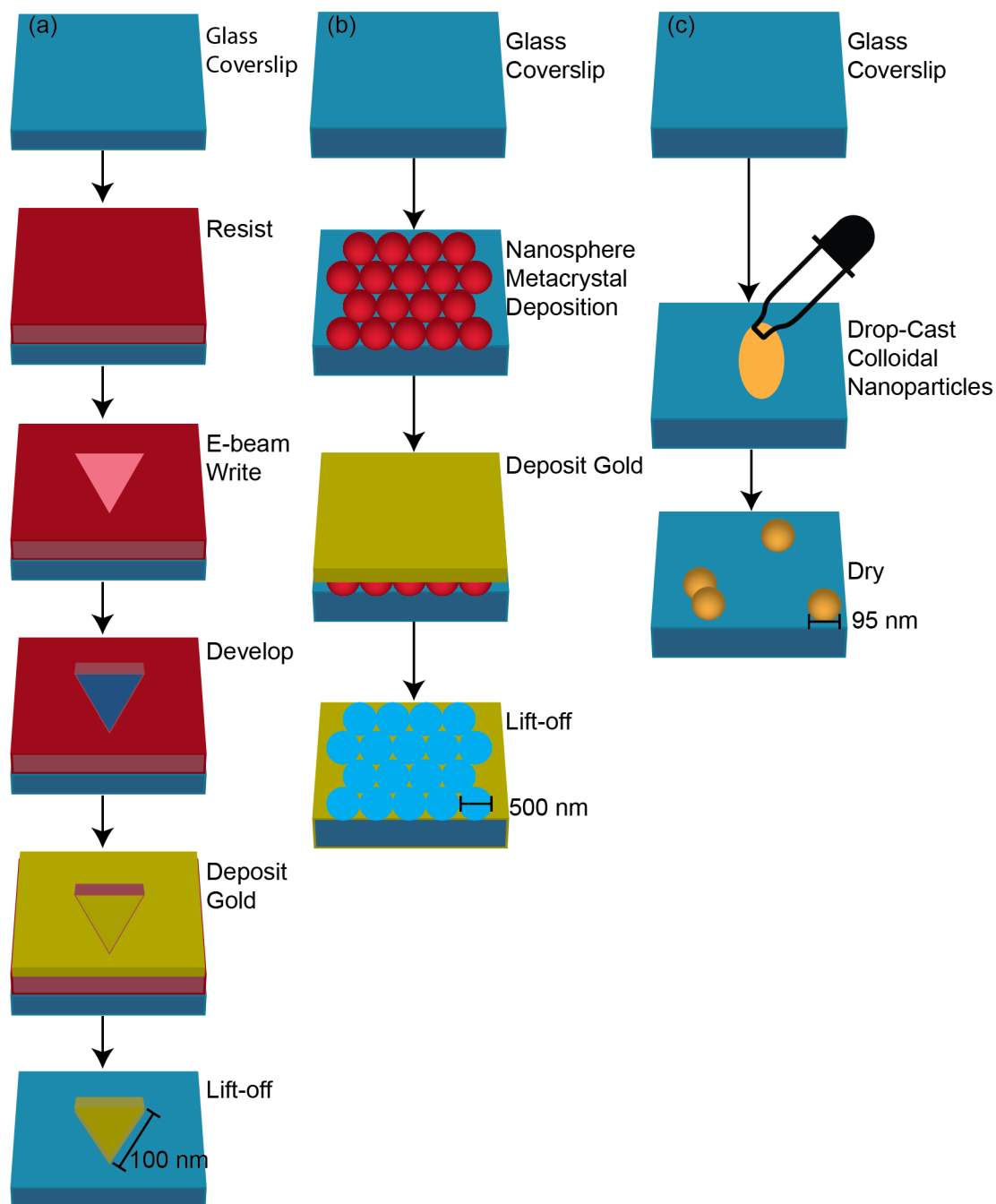
Figure 1.5: Lithography processes. (a) Electron-beam lithography process. (b) Nanosphere lithography processes. (c) Drop-casting process.

Each fabrication method was chosen for specific reasons. NSL is a cheap and easy method for making large arrays of nanotriangles. The nanotriangle sizes and interparticle distances are controlled by the size of sphere used to make the NSL mask. EBL can be used to fabricate nearly any size, shape, and pitch desired, within the resolution of the instrument. A large parameter space is available to find the optimal size, shape, and array spacing to achieve highest enhancement. Drop-casting was used to obtain single, monodisperse, chemically synthesized particles. Chemically synthesized particles are beneficial because they have much sharper resonances than the polycrystalline NSL or EBL particles, and, in this case, are spherical for theoretical modeling and simulation where symmetry can be invoked to decrease simulation time. Additionally, the drop-cast particles were used with a labeled grid, which allowed for repeated experiments on the same particles and correlated characterization. Each experiment has certain requirements, thus, choosing the appropriate fabrication is important to the design of the experiment.

1.3.2   Bottom-up lithography

One of the simplest ways to fabricate a plasmonic substrate is with bottom-up lithography by simply drop-casting colloidal nanoparticles onto a glass coverslip. The end result will be a random array of nanoparticles with spacing and clustering dependent on the concentration of particles deposited on the surface. This method is by far the fastest and easiest way to make a sample, but it lacks any array order, contains both single particles and clusters of particles of differing populations, and the particle size distribution is dependent on the particles used from the stock colloid. This method of bottom-up fabrication is useful if the goal is to have many particles from a well defined size and shape distribution. The drawbacks are that the particles need to be carefully selected for single-particles, since dimers and oligomers exist, anisotropic nanoparticles will be randomly oriented, and the particles cannot be easily revisited for correlated experiments without fiduciaries (Figure 5.1). Simply drop-casting particles on a surface is easy and if the surface has been

particularly modified and/or external forces are introduced, higher order can be introduced into the final substrate. Some recent methods for introducing order in drop-cast bottom-up lithography include using template assistance and electrophoretic [34,35] or optical [36–38] forces.

1.3.3 Top-down lithography

In contrast to bottom-up lithography, top-down lithography is used to make nanoparticles by removing material to make the final product. Common top-down lithography methods for fabricating nanoparticles include electron- or ion-beam lithography and photolithography, where features are chemically formed in a "resist" which appear after development [39], or etched directly in the material as in the case of electron or ion milling. The advantages of top-down methods include fine control over array structure and shape of the nanoparticles and the ability to have many nanoparticle sizes and shapes on a single substrate. The draw-backs are that it is often time-consuming and expensive, with individual substrates costing in excess of $200 to fabricate, and the particles themselves are not as ideal, exhibiting polycrystallinity and defects.

1.3.4 Combination approaches

The lithography classes listed above need not be mutually exclusive. In fact, many successful methods for fabricating nanoparticles use a combination of both approaches. Stencil lithography for instance uses an EBL fabricated substrate as a shadow mask for evaporating metal through to make nanoscopic features on a new substrate behind [40]. NSL can be used as a combination approach, where the bottom-up formed nanosphere metacrystal can be etched and used as a mask for metal deposition to form nanohole arrays [41]. In fact, many of the new bottom-up approaches rely on top-down methods in order to self-assemble the particles, such as in template assisted methods, where the template has been fabricated with a top-down lithography method [34, 37, 38].

1.4 Thesis Outline

In this thesis, I used plasmonic nanoparticle arrays of various size, shape, and array structure to optimize the enhancement of fluorescent proteins in living *Vibrio cholerae* cells (Chapter II). In Chapter II, gold nanotriangle array (NTA)s on glass coverslips were used as inexpensive, facile, and broadly applicable imaging substrates for living *Vibrio cholerae* cells expressing photoactivatable fluorescent proteins—the red PAmCherry or the green PAGFP—and resulted in fluorescence enhancements upon coupling living cells to nanotriangle (NT)s. Within the requirements for this wide-field coupling geometry, I analyzed and optimized the coupling as a function of local surface plasmon resonance frequency and particle coverage and determined that particles with strong scattering and good resonance overlap with the fluorophore and dense arrays provide largest enhancement. I extended upon the conclusions of Chapter II and fabricated various AuNP arrays with EBL to systematically examine the live-cell single-molecule fluorescence-enhancement toward optimal enhancement. These results demonstrate that plasmonic nanoparticle arrays can be used to enhance the fluorescence emission intensity within living cells and that the size and interparticle spacing must be carefully tuned for optimal fluorescence intensity enhancement.

I also used single-molecule super-resolution imaging to characterize the emission spectrum reshaping of dye/nanoparticle coupled systems. In Chapter III, I uncovered the distance and spectral dependence of single-molecule emission spectrum reshaping for four different fluorophores and complemented experiment with electromagnetic simulations to better understand the effects of plasmonic nanoparticle (NP)s on nearby fluorescent emitters. These results demonstrate the power of single-molecule hyperspectral imaging and may be used to improve analytical models of plasmon/dye coupling.

Finally, in Chapter IV I used single-particle super-resolution imaging to study the temperature dependence of gold nanoparticle photoluminescence toward the development of an all-fluorescence, absolute nanothermometer. The method developed here, will enable

accurate measurements of the photothermal conversion of AuNPs and their immediate surroundings.

Interplay of Nanoparticle Resonance Frequency and Array Surface Coverage in Live-Cell Plasmon-Enhanced Single-Molecule Imaging

2.1 Abstract

[1] Super-resolution imaging has provided new insights into nanoscale optics. Plasmonic gold nanotriangle arrays created by nanosphere lithography can enhance single-molecule fluorescence intensity to further improve imaging. Here, gold nanotriangle arrays on glass coverslips were used as inexpensive, facile, and broadly applicable imaging substrates for living Vibrio cholerae cells expressing photoactivatable fluorescent proteins—the red PAmCherry or the green PAGFP—and resulted in fluorescence enhancements upon coupling living cells to nanotriangle arrays. Within the requirements for this wide-field coupling geometry, we analyze and optimize the coupling as a function of local surface plasmon resonance frequency and particle coverage.

2.2 Introduction

Super-resolution fluorescence imaging has greatly improved our understanding of both light-matter interactions and biological mechanisms by taking the resolution of far-field optical microscopy down to the nanometer scale [11, 42–45]. Recently, super-resolution fluorescence imaging has been used to map the effect of plasmonic nanoparticles on localization position [29, 33, 46, 47], to describe the activities of proteins in living mammalian plasma membranes [48], and to measure biomolecule dynamics in bacterial cells [49–51]. Single-molecule microscopy beats the standard diffraction limit of light by super-localizing probes with a precision that depends on many factors; given a particular experimental setup where the microscope and detector components are fixed and the wavelength and intensity of the excitation source have been optimized, the most controllable experimental parameter is the brightness of the fluorescent label (fluorophore) [24, 52]. Fluorophore brightness can be controlled by increasing the extinction coefficient or the quantum yield via novel dye synthesis or fluorescent protein engineering [53, 54]. Alternatively, the optical properties of a fluorophore can be changed by augmenting the local dielectric constant around the fluorophore by changing the media [55] or by engineering the local density of photonic states, for instance by positioning the dye molecule in the near field of a plasmonic nanoparticle [39, 56–58]. The brightness enhancement from plasmonic coupling depends on the nanoparticle properties, including the localized surface plasmon resonance (LSPR) frequency and intensity, the nanoparticle shape and orientation, and the dye/nanoparticle separation distance [20, 59]. A desirable substrate for plasmon-enhanced super-resolution bioimaging must consider these requirements, and additionally consist of nontoxic nanoparticles that cover a large surface area and that are sufficiently dense without touching since charge transfer between nanoparticles leads to blinking which precludes single-molecule detection (Figure 2.1) [45]. Plasmon-enhanced fluorescence has been known for a long time [60], but its application to super-resolution imaging has only been realized recently [28, 39, 46, 61] and its use in cellular single-molecule super-resolution
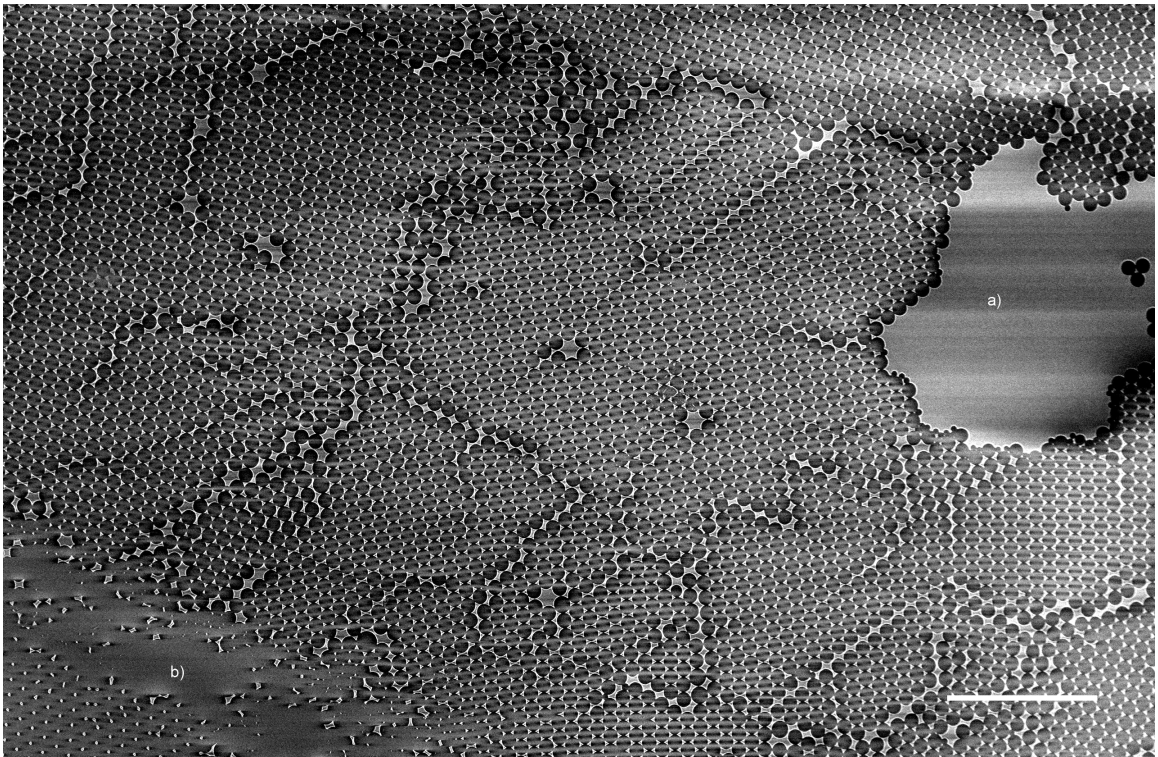
Figure 2.1: Large field-of-view scanning electron micrograph of NTA1000 showing nanotriangles that cover a large surface area without touching. Region a) is flat gold. Region b) is flat glass. Scale bar is 10 μm.

imaging has thus far been limited [62]. In this chapter, we show that the fluorescence inten-sity of nanoparticle-coupled, membrane-bound fluorescent proteins (the red PAmCherry and the green PAGFP) can be enhanced for improved live-cell super-resolution imaging by tuning the surface coverage and LSPR frequencies of gold nanotriangle arrays made by nanosphere lithography.

2.3 Experimental Section

2.3.1 Nanotriangle array fabrication

Microscope coverslips were coated with nanotriangle arrays (NTAs) using nanosphere lithography (NSL) [41]. Polystyrene latex nanospheres of 550, 746, or 990 nm diameter (coefficient of variance < 3%) (Polysciences, Inc.) were drop-cast onto O_2 plasma-etched (PE 50, PlasmaEtch Inc.) glass coverslips (Fisher Scientific) for monolayer sphere coverage, and dried under ambient conditions. The nanosphere-on-glass substrates were coated by electron beam evaporation (Enerjet Evaporator, Denton) with a 5 ± 1 nm Ti wetting layer followed by 100 ± 4 nm of gold. The polystyrene nanospheres were dissolved using Remover PG (Micro-Chem Corp.), leaving the Ti/Au NTAs adhered to the glass.

2.3.2 Nanotriangle array characterization

Each NTA-coated coverslip was characterized by dark-field spectroscopy (DFS) spectro-scopy and scanning electron microscope (SEM). For DFS spectroscopy, we illuminated the NTAs with white light from a tungsten lamp through a dark-field condenser (numerical aperture (NA) 1.2—1.4) and collected the scattered light with a 100× adjustable objective set to NA 0.6. The collected light was dispersed through a spectrometer (SP2300, Princeton Instruments) onto an electron multiplying charge-coupled device (EMCCD) camera (Ixon3 897, Andor Technologies, Ltd). DFS spectra were measured for 9 individual particles within each NTA (Figure 2.2), and corrected by dividing the background-subtracted nanotriangle

DFS by the bright-field white light spectrum (collected with NA = 1.3). The scattering peaks were determined by Gaussian fits (Table 1). The SEM images were taken in deceleration mode: 2.5 kV acceleration, 1 kV landing, 7 A current (SU8000, Hitachi High Technologies America, Inc.) to obtain overall array morphology (Figures 2.1 and 2.3), and the average nanoparticle edge length is the average edge length for each of 34–89 nanotriangles.

Table 2.1: Nanotriangle Array Characteristics[2]

NTA	NT edge length (nm)	NT surface coverage (nps/μm^2)	LSPR peaks (nm)
NTA500	$178 \pm 9, n = 89$	10.2	$565^b, 771^a$
NTA750	$223 \pm 7, n = 61$	4.5	$556^c, 632^b, 1000^a$
NTA1000	$327 \pm 10, n = 34$	2.6	$570^d, 683^c, 900^b, >> 1000^a$

2.3.3   *Vibrio cholerae* growth

O395 *V. cholerae* expressing fusions of photoactivatable fluorescent proteins to inner membrane-bound proteins (TcpP-PAmCherry or ToxR-PAGFP; strains CS23 and CS34, respectively) were grown to OD 0.6 at 37 ^{o}C in LB media at pH 8.5 with shaking overnight. The cultures were then diluted 500-fold in LB at pH 6.5 and incubated with shaking at 30 ^{o}C for 4 h to induce fusion protein expression. The cells were concentrated by centrifuging at 10,000 rpm for 1 min at 25 ^{o}C.

2.3.4   Single-molecule cellular imaging

The concentrated cells were prepared for imaging by sandwiching 2 μL of concentrated culture between a 2% agarose in M9 minimal media (pH 6.5) gel pad and either a reference glass coverslip (PE 50, PlasmaEtch Inc.) or an NTA-coated coverslip. The *V. cholerae* cells were imaged at room temperature on a wide-field inverted microscope (Olympus IX71) with a 1.4 NA, 100× oil-immersion phase-contrast objective. Phase-contrast images were

---

[2]NTA500, NTA750, and NTA1000 refer to the polystyrene latex nanosphere diameters (in nm). Edge lengths are measured by SEM of at least 34 NTs per array. LSPR frequencies measured by dark-field spectroscopy. [a]First LSPR peaks in the order of appearance. [b]Second LSPR peaks in order of appearance. [c]Third LSPR peaks in order of appearance. [d]Fourth LSPR peaks in order of appearance.
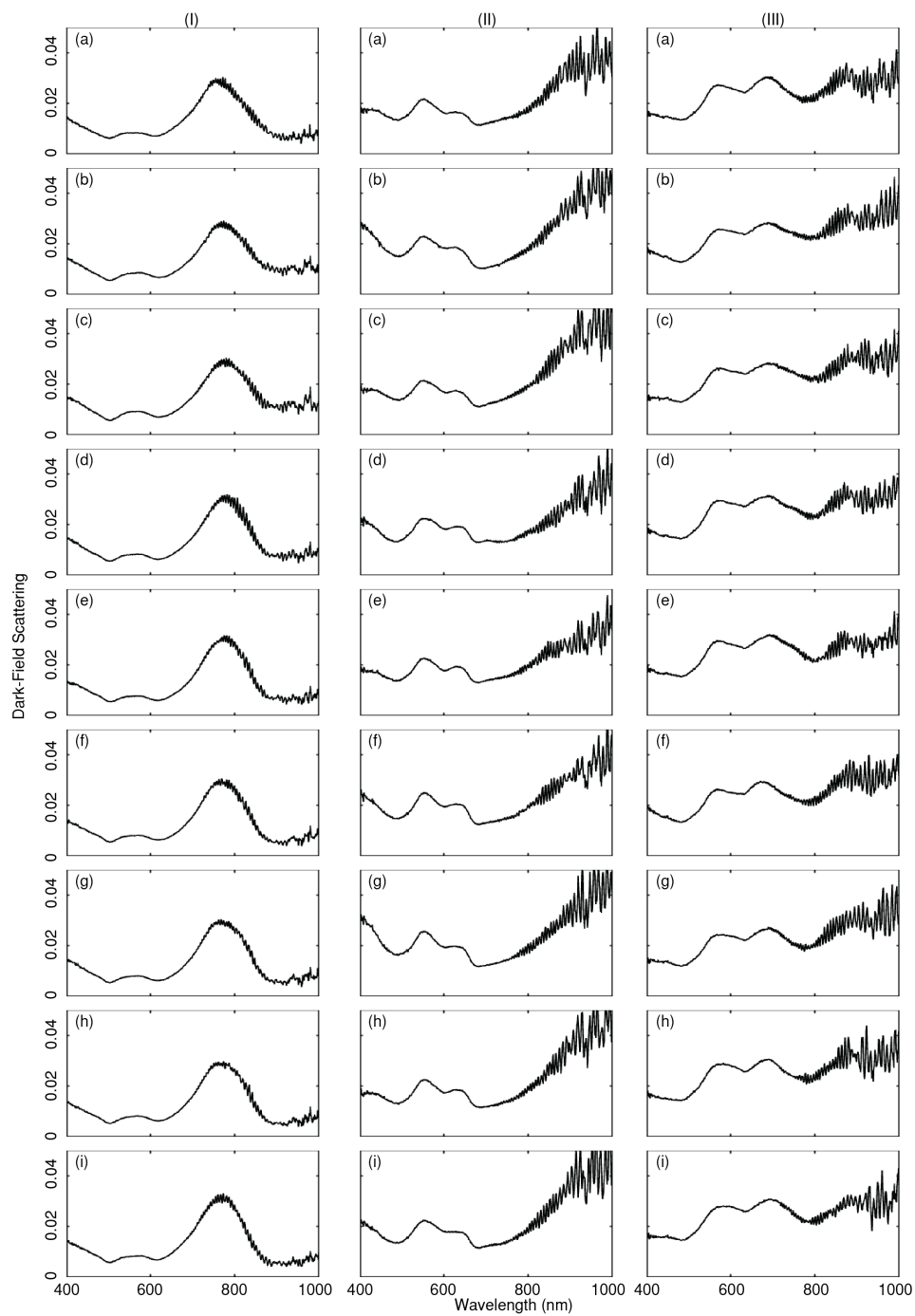
Figure 2.2: Nine representative single-particle dark-field scattering spectra for each of (I) NTA500, (II) NTA750, and (III) NTA1000. These spectra are averaged to give the dark-field plots in Figure 2.5 d–f, respectively.
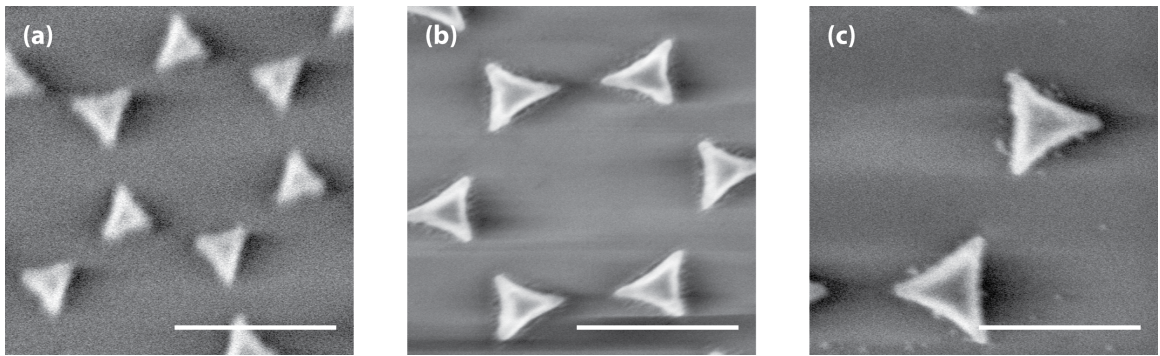
Figure 2.3: Scanning electron micrographs of (a) NTA500, (b) NTA750, and (c) NTA1000 at 200,000× magnification. Scale bars are 500 nm.

obtained with white light illumination through a phase condenser (Figure 2.4). Single molecules of TcpP-PAmCherry or ToxR-PAGFP were photoactivated in cells with a 70–100 ms exposure to a 405 nm CW laser (0.06 μW/μm^2; Coherent Cube) and then imaged at 25 fps under continuous 3.9 μW/μm^2 excitation by a 488 nm CW laser (Sapphire, Coherent) for PAGFP or a 561 nm laser (Sapphire, Coherent) for PAmCherry, until photobleaching was observed ($\leq$5 s). The cycle of photoactivation and imaging was repeated for 5 minutes. We ensured that only isolated single molecules were detected by using this low 405 nm activation intensity such that only 1-2 molecules per cell were photoactivated per activation cycle.

2.3.5   Single-molecule intensity analysis

The SMALL-LABS algorithm was used to detect single fluorescent molecules in the fluorescence images and to subtract accurate backgrounds. Briefly, for every detected molecule, the local accurate background was the average of all imaging frames in which no molecules were detected in the vicinity of that molecule. This local background was subtracted from the raw image, and the background-corrected integrated intensity was the sum of the background-corrected pixel intensities over 15 $\times$ 15 image pixels (735 $\times$ 735 nm; i.e., a diffraction-limited area from the molecule center). The enhancement factors for each NTA size were calculated from the ratio of the mean single-molecule integrated intensity in cells on NTA to the mean single-molecule integrated intensity in cells on a clean coverslip. The error on the mean was determined by Monte-Carlo bootstrapping with 1000 bootstraps, and that error was propagated through for the error on the enhancement factor.
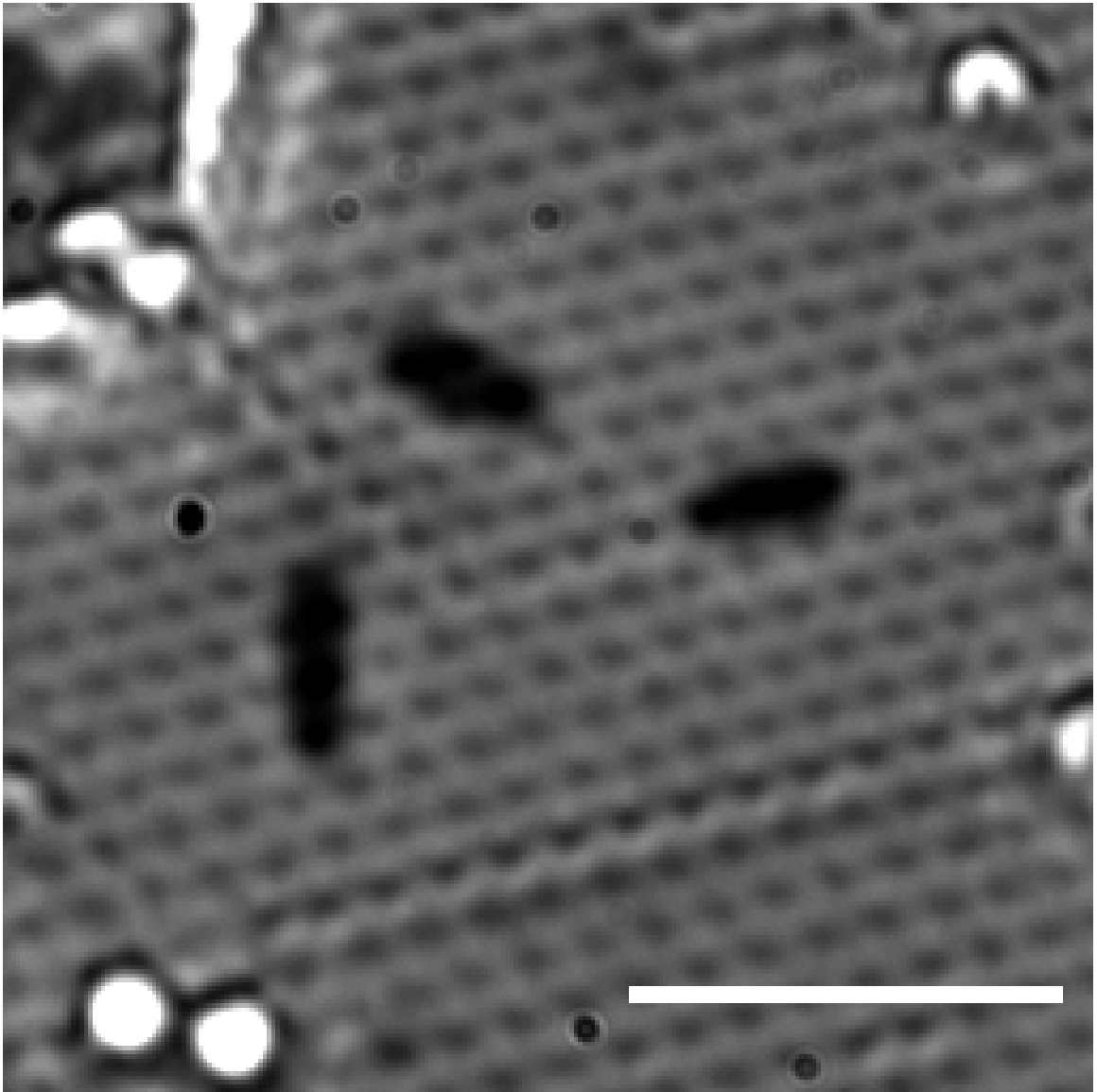
Figure 2.4: Phase contrast image of *V. cholerae* on NTA750 array. Scale bar 5 μm

2.4 Results and Discussion

2.4.1 NTA coated coverslips

Gold NTAs were fabricated on glass coverslips via NSL with varying nanosphere diameters [63]. Because the nanotriangles (NTs) are formed at the interstitial spaces between the nanosphere mask, the NT size and surface coverage depend on the nanosphere diameter [41]. The NTA morphologies were characterized with SEM (Figure 2.5a–c and Figure 2.3) to determine the NT edge length and array coverage for each NTA (Table 2.1). Larger nanospheres used for the NSL deposition mask lead to larger NTs which have lower resonance frequencies, due to decreased surface plasmon confinement, but higher scattering intensities, due to their size [41, 64]. Average DFS spectra for each of the NTAs are plotted in Figure 2.5d–f and the peak wavelengths are listed in Table 2.1; single NT DFS spectra are plotted in Figure 2.2. As expected, when the nanosphere diameter increases, the NT size increases while concurrently, the number of particles per area decreases. Additionally as the NT size increases, so do the scattering intensity and the number of visible LSPR modes, and each LSPR mode red-shifts. The NTA-coated coverslip made from the smaller (500 nm NSL) mask has the greatest number of particles per area (Table 2.1), but it also has a much lower scattering intensity in the 540–640 nm range that provides overlap with the excitation and emission spectra of PAmCherry (Figure 2.5a). Conversely, NTA1000 has only one quarter the number of NTs per area relative to NTA500, but an approximately 4-fold greater scattering intensity in the 540–640 nm range.

2.4.2 Plasmon-enhanced live-cell fluorescence imaging

Vibrio cholerae is a human pathogen and causative agent in the disease cholera. *V. cholerae* pathogenicity is due to the secretion of cholera toxin, expression of which is regulated by the transcription activators TcpP and ToxR, two inner membrane proteins [65]. Imaging single molecules in living cells allows for a more complete understanding of the
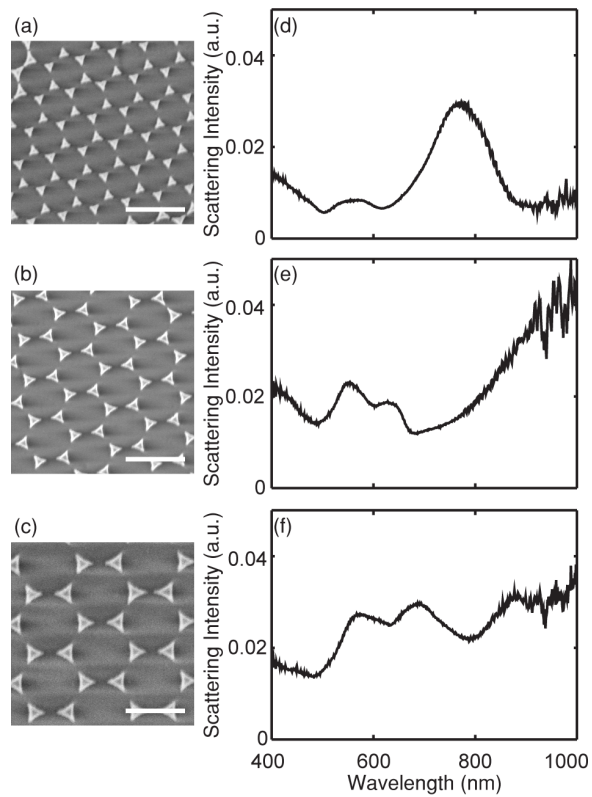
Figure 2.5: SEM of (a) NTA500, (b) NTA750, and (c) NTA1000 NT arrays (scale bars: 1 μm). The measured NT side lengths are tabulated in Table 2.1. (d–f) Average DFS spectra of nine single-particle spectra for each gold NTA. Individual DFS spectra presented in Figure 2.2. Peak positions tabulated in Table 2.1.

dynamics and mechanisms involved in biochemical pathways, such as the role of TcpP in *V. cholerae* virulence [66]. When *V. cholerae* cells are placed on top of extracellular nanoparticles, TcpP-PAmCherry is perfectly positioned for plasmon-enhanced single-molecule fluorescence imaging because it is localized to the inner membrane, roughly 20 nm away from the plasmonic NTA and well within the enhanced near field. PAmCherry also has fluorescence excitation and emission maxima of 564 nm and 595 nm, respectively; [67] these wavelengths overlap well with the NTA LSPR frequencies (540–640 nm). The fluorescence intensity distributions from all TcpP-PAmCherry single-molecule localizations in living *V. cholerae* cells on NTA-coated coverslips were compared to localization in cells on bare reference coverslips to determine the average brightness enhancement for NT-coupled PAmCherry in living cells (Figure 2.6). The intensity distributions for the single-molecule localizations are shifted to higher intensity for cells on all NTA-coated coverslips compared to the reference. Additionally, the intensity distributions for cells on the NTA-coated coverslips are broader than the distribution for bare glass. This distribution broadening is largely due to the distance dependence of plasmon-enhanced fluorescence leading to heterogeneous enhancement [68].

Obvious enhancements were seen for all of the NTA-coated coverslips, but NTA500 provided the largest average enhancement (greater than two-fold). The average enhancement factor depends on many variables including the overlap between the fluorescence emission and LSPR frequencies [31,69], the LSPR mode strength [70], and the NT coverage. Because of this combination of factors, the degree of enhancement can be difficult to predict, although our results point toward maximal enhancement when the surface coverage is increased while maintaining some resonance overlap and some moderate resonance intensity at the resonance frequency.

The effect of surface coverage on fluorescence enhancement was further investigated by measuring the single-molecule fluorescence intensity enhancement for ToxR-PAGFP in living *V. cholerae* cells upon coupling to the NTA500 and NTA1000 NTA-coated coverslips

27

Figure 2.6: Fluorescence intensity distributions of membrane-bound TcpP-PAmCherry molecules in *V. cholerae* cells imaged on glass coverslips (white) and on NTA-coated coverslips (grey) for (a) NTA500, (b) NTA750, and (c) NTA1000. The nanoparticle-coupled TcpP-PAmCherry molecules are enhanced by a factor of 2.13 ± 0.05, 1.38 ± 0.02, and 1.59 ± 0.03 in (a), (b), and (c), respectively.

(Figure 2.7). Since PAGFP excitation and emission maxima are at 502 nm and 516 nm, respectively [71], the resonance overlap between PAGFP and the NTAs is small. Still, there is a modest ~1.2-fold enhancement, and the NTA500 array leads to a slightly larger enhancement due to its denser NTA coverage (Table 2.1). Overall, these results indicate that a large parameter space exists within which to obtain optimal fluorescence enhancement for live-cell imaging. In the case of PAmCherry, where the LSPR and fluorescence spectra overlap (Figure 2.6), good enhancement is observed. The LSPR intensity and NTA surface coverage both have significant effect on overall enhancement: NTA500, which has high NTA coverage (Table 2.1), and NTA1000, which has high LSPR strength (Figure 2.5), have greater average enhancements than NTA750, which is intermediate between the two. In the case of PAGFP, whose fluorescence spectrum overlaps very little with the gold LSPR, despite the absence of resonant coupling, the enhancement is nearly the same for NTA500 and NTA1000, if only slightly higher for NTA500.

2.5   Conclusions

Single-molecule fluorescence imaging has improved our understanding of biological mechanisms and light-matter interactions [31, 72]. Since the localization precision of single-molecule super-resolution methods is limited by the number of photons collected from the fluorophore, any increase in the emission intensity can significantly impact the quality of the data. Here, we have demonstrated by fabricating gold NTAs with nanosphere lithography that fluorescence enhancements of the red photoactivatable fluorescent protein PAmCherry in excess of two-fold are accessible for live-cell single-molecule fluorescence imaging. Moreover, we have uncovered an important tradeoff in this sample geometry between LSPR strength and the NTA surface density. Finally, we have shown that some fluorescence enhancement is attainable for the green fluorescent protein PAGFP, but that in the absence of resonant coupling, this enhancement is much more modest. Overall, the ability to use simple, inexpensive plasmonic substrates to produce enhanced single-
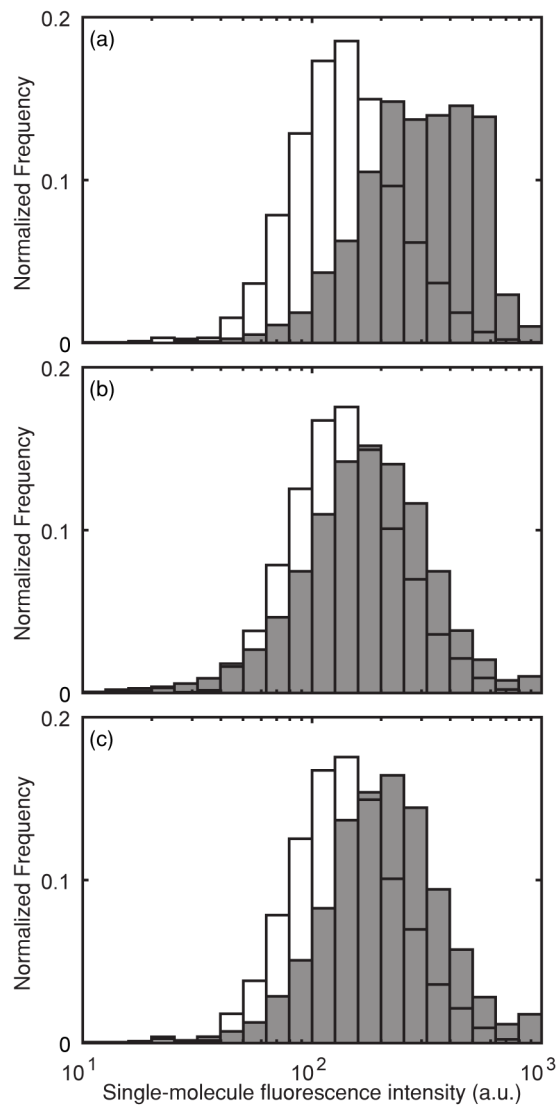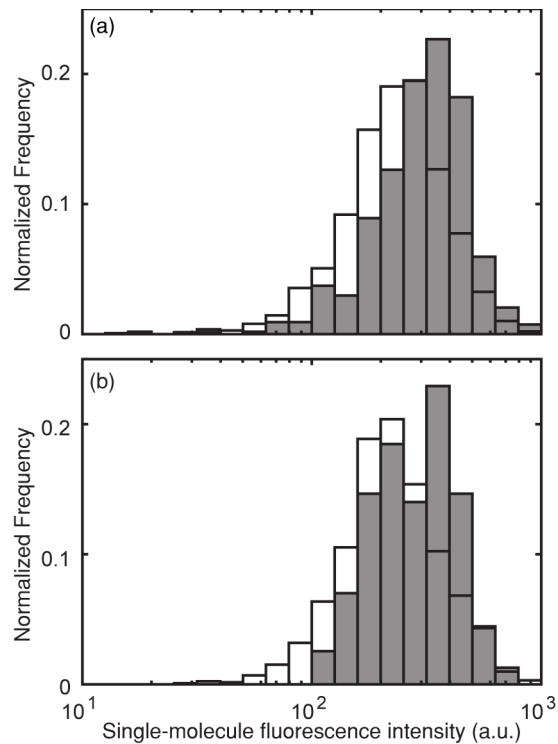
Figure 2.7: Fluorescence intensity distributions of membrane-bound ToxR-PAGFP in *Vibrio cholerae* cells imaged on glass coverslips (white) and on NTA-coated coverslips (grey) for (a) NTA500 and (b) NTA1000 (gray). The nanoparticle-coupled ToxR-PAGFP is enhanced by a factor of 1.28 ± 0.03 and 1.21 ± 0.04 in (a) and (b), respectively.

molecule fluorescence will be immediately applicable in the life sciences, while at the same time it is clear that alternative, more costly solutions that allow careful selection of NTA characteristics such as particle size, shape, and coverage will yield much greater than two-fold single-molecule fluorescence enhancements in live cells.

2.6   Toward Optimal Live-Cell Plasmon-Enhanced Fluorescence

Single-molecule super-resolution fluorescence imaging has enabled sub-diffraction-limited imaging in living cells, leading to an improved understanding of biological processes previously obscured by ensemble and *in vitro* methods [49]. Additionally, plasmon-enhanced fluorescence has demonstrated that the emission intensity of coupled fluorescent proteins can be improved through resonant-enhancement of the fluorophore excitation and emission [28, 30]. Previous approaches to live-cell plasmon-enhanced fluorescence imaging have used NSL fabricated nanotriangle arrays [30, 62] and stencil lithography fabricated bowtie nanoapertures [40] as enhancement substrates. Although we were able to realize enhancement factors in excess of 2-fold, the fabrication process did not allow for independent control of the particle resonance frequency and surface coverage. Here, we expand upon the previous results to develop figures of merit for designing a plasmonic substrate for optimal enhanced, live-cell imaging. The major factors for optimizing the enhancement of live-cell fluorescence imaging are, nanoparticle size and shape, and the nanoparticle array morphology: inter-particle spacing and array packing. Thus, we use electron-beam lithography (EBL) to fabricate a variety of gold nanoparticle (AuNP) arrays in which the particle size and shape (and thus the LSPR modes can be tuned separately from the surface coverage.

2.6.1 EBL experimental design

2.6.1.1 Plasmonic substrate preparation

24 sets of nanoparticle arrays (NPAs) were designed with different sizes, shapes, array order, and center-to-center distance (pitch) (Table 2.2).

Table 2.2: EBL Nanoparticle Array Combinations

Nominal Nanoparticle size (nm)[3]	Pitch (nm)	Array order	Nanoparticle type
70, 90, 110, 130	250, 300, 1000	Square, Hexagonal	Circle, Triangle

Microscope coverslips were coated with NPAs using EBL. A 200 nm poly(methyl meth-acrylacte) (PMMA, Michrochem) layer was spin coated onto a glass coverslip. A 5 nm sacrificial gold film was thermally deposited onto the PMMA to ground the surface (Angstrom Engineering, Evovac Evaporator), then the sample was exposed to the e-beam, 100 kV, 940–1040 pA (JEOL JBX 6300FS). The exposed substrate was developed by removing the sacrificial gold layer with gold etch (KI and iodine complex), soaking in 1:3 MiBK:IPA, rinsing in IPA and finally cleaned with O_2 plasma descum (YES Plasma Etch). The substrate was coated with a 5 ± 1 nm Ti wetting layer followed by 50 ± 4 nm of gold through electron beam evaporation (Denton Enerjet Evaporator). The PMMA resist was dissolved overnight using Remover PG (Micro-Chem Corp.) followed by sonication, leaving the Ti-Au nanoparticles adhered to the glass.

2.6.1.2 EBL nanoparticle array characterization

Each array's LSPR mode was measured using DFS spectroscopy to determine which arrays have good spectral overlap with PAmCherry and PAGFP (500–600 nm) and large LSPR intensity for enhanced live cell imaging (Figure 2.8). The substrate was illuminated with a water immersed dark-field condenser (NA = 1.2–1.4) and collected through a 40× 0.95 NA objective (Olympus UPLSAPO 40X2).

---

[3]Size is diameter for circles and edge length for the equilateral triangles
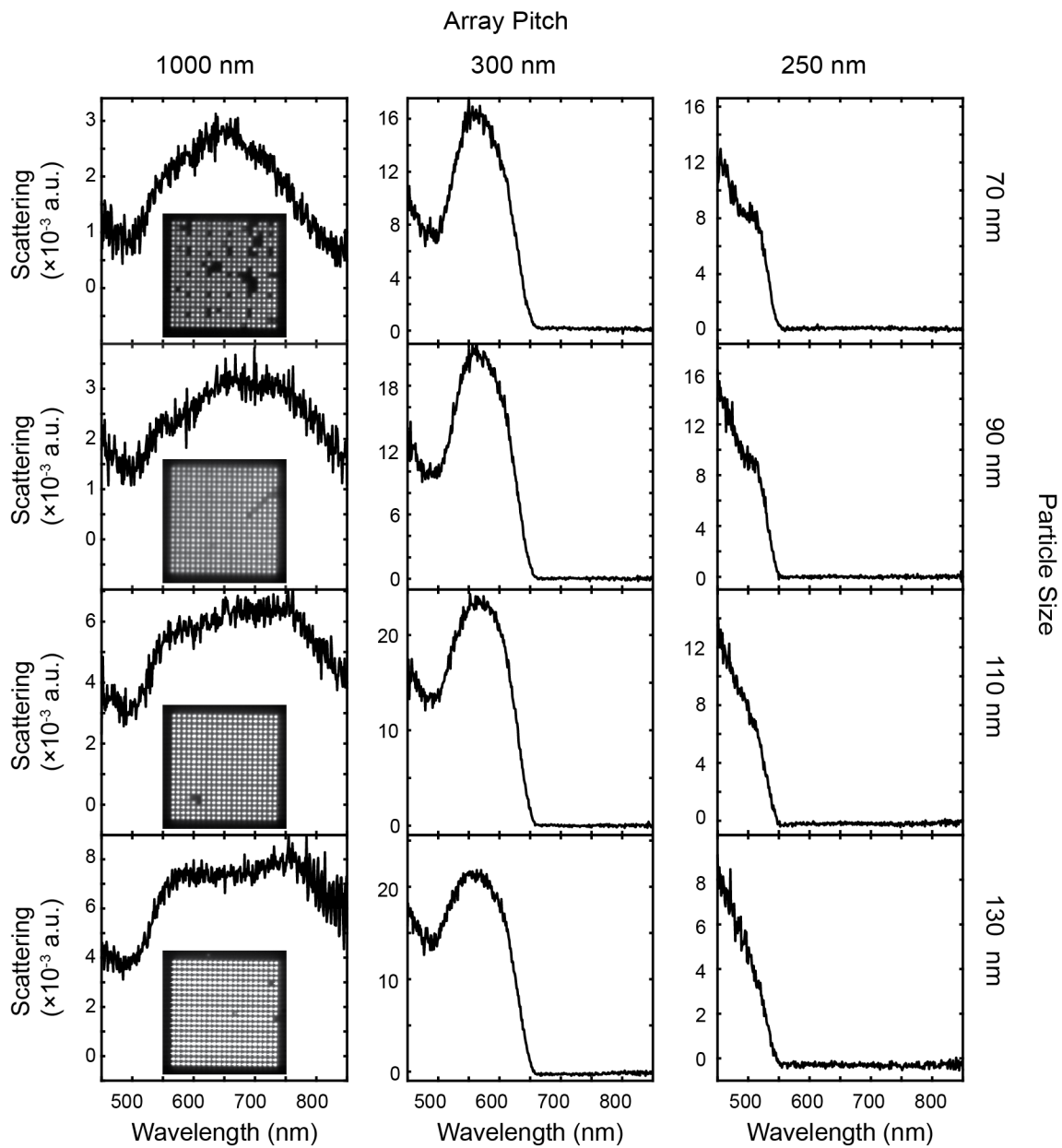
Figure 2.8: Dark-field scattering spectra of EBL circle nanoparticle arrays of different sizes and array pitches. Insets, dark-field image of the array for each given spectrum. Darkfield images are 245 μm by 245 μm.

For the square arrays of circular nanoparticles in the 1000- and 300-nm array pitch (columns 1 and 2 in Figure 2.8), the scattering intensity increases with particle size. This increase is due to the increase physical cross-section and thus scattering cross-section. On the other hand, in the 250-nm array pitch column, the the trend is reversed: increasing particle size leads to a decrease in scattering intensity. This decrease in scattering intensity could be due to either a grating effect or increased reflectivity, either of which cause the light to be scattered at angles not collected by the objective. Also, as the array pitch decreases, we see that the scattering spectrum blue-shifts rapidly, thus there is tunability in the scattering band of the nanoparticle arrays by changing the pitch. In addition to the blue shift, there is also an increase in the scattering intensity. This scattering increase could be due to the increased particle density as well as formation of lattice plasmon modes [73].

2.6.2 Future outlook

The results from the DFS analysis of the nanoparticles indicate that a circular nanoparticle of 130 nm and an array pitch of 300 nm should be a good substrate for plasmon-enhanced live-cell imaging of PAmCherry. Further improvements in the fabrication process are being pursued to obtain arrays of triangular nanoparticles that lack large defects to compare the LSPR mode strengths between circles and triangles. Finally, the substrates with high LSPR strength and large particle densities will be used for live-cell enhancement studies to measure the enhancement factors for each array.

CHAPTER III

Single-Molecule Emission Spectrum Reshaping

3.1 Abstract

The radiation characteristics of fluorescent molecules are highly susceptible to their local environment. Gold nanoparticles modify the local environment through a wavelength-dependent redistribution of local electric field intensity and local density of (photonic) states (LDOS). Thus, fluorescent molecules in the near field of plasmonic nanoparticles can experience changes in their intrinsic fluorescence spectrum leading to a reshaping of the emission spectrum. The heterogeneity of emission spectrum reshaping is uniquely accessible to single-molecule hyperspectral imaging, as ensemble averaging is avoided and both the super-resolved position of the fluorophore and its emission spectrum can be measured simultaneously. Here, we demonstrate single-molecule fluorescence emission spectrum reshaping upon near-field coupling to individual spherical gold nanoparticles using hyperspectral super-resolution fluorescence imaging and we resolve this spectral reshaping as a function of the spectral overlap and separation distance dependence between the nanoparticle and the dye. We find that dyes bluer than the plasmon resonance maximum are red-shifted and dyes redder than the plasmon resonance maximum are blue-shifted. Spectral reshaping shifts the primary vibronic peaks and changes the ratios of vibronic transition probabilities to favor secondary vibronic peaks, leading to effective emission maxima shifts in excess of 50 nm. These results illustrate the power of super-

resolution hyperspectral imaging and full-field, full-spectrum electromagnetic simulations for studying light-matter interactions.

3.2 Introduction

Single-molecule super-resolution imaging is a powerful technique that can elucidate heterogeneities and uncover hidden or rare events that would otherwise be lost in ensemble measurements, while also improving the image resolution by localizing the fluorophore emission below the diffraction limit of light [42, 43, 74]. These attributes make single-molecule super-resolution imaging indispensable for directly measuring the light-matter interactions of metal nanoparticles and fluorophores. gold nanoparticles (AuNPs) are particularly interesting in their ability to act as chemically stable optical antennas that couple propagating light from free space to the near field through the resonant collective oscillation of conduction band electrons known as a localized surface plasmon resonance (LSPR) [17, 20]. The wide range of applications of noble metal nanoparticle LSPRs include enhanced spectroscopies [30,75,76], enhanced solar light collection [77], hot-electron/hot-hole chemistry [14,78], and enhanced catalysis [79]. Fluorescence microscopy has explored many of the nuances of emitter-plasmon coupling, and single-molecule super-resolution imaging has expanded our understanding of how plasmon-coupled fluorescence depends on the dye/nanoparticle separation distance [29, 59, 80] and the dye/nanoparticle spectral overlap [31,58,81]. Plasmon-enhanced fluorescence depends both on the excitation enhancement, due to a redistribution of the local electric field around the plasmonic nanoparticle, and the emission enhancement, due to the wavelength- and distance-dependent change in the LDOS [82].

The emission spectrum of a dye in the near field of a plasmonic nanoparticle will be modified by the wavelength-dependent radiative rate enhancement of the coupled system. Since a fluorescence emission spectrum is a convolution of each vibronic transition weighted by the respective rates, the relative rates of the transitions can be augmented in

the presence of a nearby plasmonic nanoparticle, leading to emission spectrum reshaping. The distributions of emission spectrum wavelength maxima and relative intensity ratios of the vibronic transitions are highly accessible to single-molecule hyperspectral imaging [83], where both the spectrum and super-resolved position of a fluorophore can be determined, and wavelength-dependent effects of plasmonic coupling can be measured for each molecule.

3.3 Experimental

3.3.1 AuNP sample preparation

Glass microscope coverslips were labeled with 100-nm thick Ti/Au grid marks, fabricated with photolithography and physical vapor deposition (GCA, AS200 Autostep; Denton, Enerjet Evaporator), and then cleaned by argon plasma etching (PlasmaEtch PE-50) followed by sonication in 2% Hellmanex III solution (Hellma Analytics). The coverslips were rinsed with distilled de-ionized (DDI) water and dried with nitrogen. 95 nm diameter AuNPs (BBI solutions) were drop-cast onto the cleaned coverslips and dried in a vacuum oven at 50 ^{o}C. The AuNP-coated coverslips were rinsed with DDI water and dried with nitrogen.

3.3.2 Single-molecule hyperspectral super-resolution fluorescence imaging

Single-molecule epifluorescence microscopy was performed on an inverted microscope (Olympus IX-71) with a 1.4 NA 100× oil-immersion objective (Olympus UPLSAPO 100XO). Four different fluorophores were investigated: BDP-FL, BDP-R6G, Cy3, and Cy3.5 (Lumiprobe, NHS-ester conjugated). The dye was introduced by flowing 1–8 nM dye solution into a reservoir on the AuNP-coated coverslip with syringe pumps (New Era Pump Systems, Inc.); the dye solution in the reservoir was refreshed every 15 min by withdrawing the old solution then infusing new dye solution into the reservoir. Single-molecule images

and spectra were obtained by stochastic adsorption/desorption events of the dyes onto the coverslip [12]. The dyes were all excited with collimated 1–2 kW·cm^{-2} 488-nm laser illumination (Coherent Sapphire). The scattered light was collected through the objective, filtered by a dichroic mirror and long-pass filter (Semrock Di01-R488 and BLP01-488). The light was then separated into two channels—one for imaging and one for spectroscopy—by a 70R:30T beam splitter (Thorlabs BST10R). The 70% reflected light was focused through 350-nm slits in the x-dimension in image-space and dispersed through a spectrometer (Princeton Instruments SP-2300i, 150/500 nm grating) onto an electron multiplying charge-coupled device (EMCCD) camera (Andor iXon 897) with 300-ms frame exposure times. The 30% transmitted light was simultaneously imaged on a second EMCCD camera (Andor iXon 887). The second camera was triggered by the spectral imaging camera and also had an average exposure time of 300 ms. Microscope automation was performed using a custom Matlab program integrated with Micro-Manager (Figure 3.5g) [84]. The background in the single-molecule images and spectra was subtracted using the Single-Molecule Accurate LocaLization by LocAl Background Subtraction (SMALL-LABS) method: the temporal average of imaging frames where no molecules were found within the same image region was subtracted from each molecule image [85]. The background-subtracted image or spectrum was then fit for super-localization and spectral deconvolution with two-term Gaussian fitting (Equation 3.4). The substrates and syringe pump tubing were cleaned by sequential soaking in hexanes (Fisher Scientific), acetone (Acros Organics), dimethyl sulfoxide (Sigma Aldrich), and DDI water between experiments to prevent cross-contamination by the different dyes.

3.3.3 AuNP single-particle dark-field scattering spectroscopy

The AuNP-coated coverslip was immersed in DDI water and illuminated with a broadband white light source focused through a dark-field condenser (1.2–1.4 NA). The scattered light was collected through a 100× 0.6-NA oil-immersion objective and imaged on the

same hyperspectral imaging system. The scattering spectrum of each nanoparticle within a 50 × 50 μm area was measured and correlated with its position on the coverslip.

3.3.4   Finite-difference time-domain simulations

Electromagnetic simulations were performed in Lumerical FDTD Solutions software [31, 39]. To simulate the AuNP scattering spectrum, a 95-nm diameter AuNP on a glass surface (n = 1.5) surrounded by water (n = 1.3) was excited by x- and y-polarized plane waves from beneath the glass substrate. The scattering was measured as the total power transmitted through a box surrounding the entire structure, and the electric field intensity was measured in the xy-plane at 3 nm above the glass surface.

Dye coupling simulations were performed with a 95-nm AuNP in water on top of a glass surface. Here the power was not supplied by a plane wave; rather, the dyes were simulated as point electric dipoles at specific distances from the AuNP center (Figure 3.2b), and transmission boxes were used to measure the total and radiative powers (Figure 3.3). The FDTD simulation contains the information for all frequencies, which are preserved for calculating the wavelength dependent excitation and emission enhancement factors (Figure 3.1, Equations 3.1–3.3).

The reshaped spectrum of the coupled dye/AuNP pair, $F(r, \omega)$, was calculated according to Ringler et al. [82], this coupled spectrum was calculated for each dye at various dye/AuNP separations, r, based on $F_0(\omega)$, the intrinsic fluorescence emission spectrum of BDP-FL, BDP-R6G, Cy3, or Cy3.5 (Equation 3.1–3.3):

$$F(r, \omega) = F_o(\omega) \times g_{ex}(r, \omega_L) \times g_{em}(r, \omega) \tag{3.1}$$

Here, g_{ex} is the excitation enhancement factor and g_{em} is the emission enhancement factor. The excitation enhancement factor is calculated at the laser frequency, ω_L:
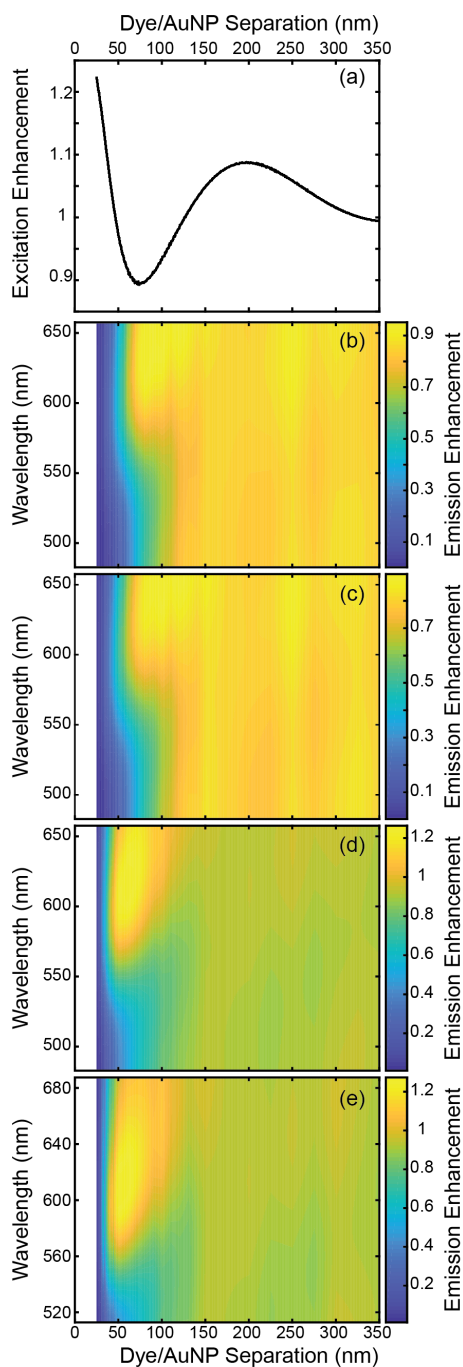
Figure 3.1: (a) Excitation enhancement function, g_{ex} in Equation 3.2, vs. dye/AuNP separation at 488 nm for a 95-nm diameter gold sphere. (b–e) Emission enhancement function, g_{em} in Equation 3.3, for (b) BDP-FL, (c) BDP-R6G, (d) Cy3, and (e) Cy3.5. The enhancement factors in the wavelength dimension remain relatively flat for dye/AuNP separations, $r > 150$ nm, but have a strong wavelength dependence for separations, $r < 150$ nm.

$$g_{ex}(r, \omega_L) = \frac{\sum_{i=x,y,z} E_i^2(r, \omega_L)}{\sum_{i=x,y,z} E_{0i}^2(r, \omega_L)} \tag{3.2}$$

where E_i^2 is the x-, y-, or z-component of the electric field intensity, and the emission enhancement is calculated as:

$$g_{em}(r, \omega) = \frac{1}{\eta_o} \frac{\frac{P_r(r,\omega)}{P_{0r}(r,\omega)}}{\int_0^\infty f(\omega) \frac{P_r(r,\omega)}{P_{0r}(r,\omega)} d\omega + \int_0^\infty f(\omega) \frac{P_{tot}(r,\omega) - P_r(r,\omega)}{P_{0r}(r,\omega)} d\omega + \frac{1}{\eta_0} - 1} \tag{3.3}$$

where P_r is the power radiated by a dipole source in the presence of the AuNP and P_{0r} is the power radiated by a dipole source in the absence of the AuNP, P_{tot} is the Purcell enhancement of a dipole near the AuNP, $f(\omega)$ is the integral normalized intrinsic emission spectrum of the dye, and η_0 is the intrinsic quantum yield of the dye.

In the finite difference time domain (FDTD) calculations, P_{tot} is measured as the total power transmitted through a box around the dipole source (green box in Figure 3.2b) and P_r is the power transmitted through a box around the source and the AuNP (purple box in Figure 3.2b) [31, 39].

The resulting excitation factor is presented as a function of r in Figure 3.1a. The emission enhancement factors, g_{em}, are plotted as a function of distance and wavelength in Figure 3.1b−e. The greatest changes in the emission reshaping occur for separation distances < 150 nm.

3.4   Results and Discussion

3.4.1   AuNP characterization

A glass coverslip substrate labeled with a grid was decorated with AuNPs by drop-casting for the series of single-molecule, single-particle measurements. The automated sample stage was scanned over a 50×50 μm area and the relative position and dark-field scattering spectrum of these 14 particles (grey points, Figure 3.2a and Figure 3.3) were

41

measured; these spectra matched the LSPR peak from a FDTD simulation of a 95-nm AuNPs in water on glass excited by a plane wave (black curve, Figure 3.2a).

3.4.2 Single-molecule hyperspectral super-resolution fluorescence imaging

The AuNPs were visualized by hyperspectral microscopy (Figure 3.5) to obtain their super-resolution position (Figure 3.5a) and single-particle photoluminescence spectrum (Figure 3.5b,f). Four fluorescent dyes—BDP-FL, BDP-R6G, Cy3, and Cy3.5—each with different overlap between their emission spectrum and the AuNP scattering spectrum (Figure 3.2a), were excited with 488-nm light to measure spectral reshaping upon plasmonic coupling. In each experiment, a dilute (1 − 8 nM) solution of one dye was placed over the substrate, and single-molecule images and spectra upon stochastic adsorption of dye molecules onto the coverslip [12]. Hyperspectral single-molecule localizations were made by simultaneously imaging the single molecules (Figure 3.5c) and acquiring the single-molecule fluorescence emission spectra (Figure 3.5b,d,e). Thus, in the super-localized hyperspectral images of each molecule, each molecule location was compared to the position of the nearest gold nanoparticle to obtain the dye/nanoparticle separation distance (distance r from the AuNP center x position as shown in Figure 3.2b). The plasmon-coupled dye emission enhancement was calculated in FDTD simulations of point electric dipoles at a distribution of dye/AuNP separation distances (red stars in Figs.3.2b and 3.4). This wavelength-dependent emission enhancement was multiplied in wavelength space by the intrinsic dye fluorescence spectrum to simulate the separation-dependent plasmon-coupled dye emission spectrum, according to Equations 3.1–3.2 [82].

For each of the four dyes, the intrinsic dye spectrum was measured from the average of the emission spectra of all molecules with dye/AuNP separation distances greater than 700 nm (blue curves in Figure 3.6. The experimental and simulated coupled emission spectra were measured for each separation distance; to increase the signal-to-noise ratio, the experimental spectra for all dye/AuNP separation distances within 40-nm bins were aver-
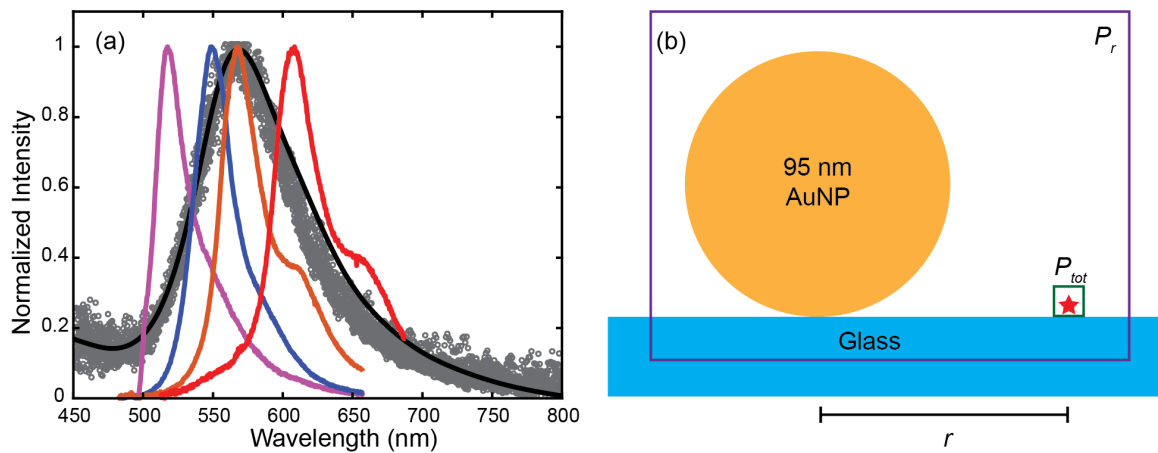
Figure 3.2: (a) Normalized aggregate experimental (grey circles) and FDTD simulated (black line) scattering spectra of 95-nm diameter AuNPs. Normalized BDP-FL, BDP-R6G, Cy3, and Cy3.5 emission spectra (magenta, blue, orange, and red, respectively). Excitation wavelength: 488 nm. (b) Side view of the FDTD dipole simulation geometry. A point electric dipole (red star) is simulated in water (white; $n = 1.3$) 3 nm above a glass surface (blue; $n = 1.5$) and r nm from a gold sphere (diameter = 95 nm). The transmitted power is measured through boxes around the dipole source (green box) and dipole/AuNP system (purple box) to measure P_r and P_{tot}, respectively, in Equation 3.3.
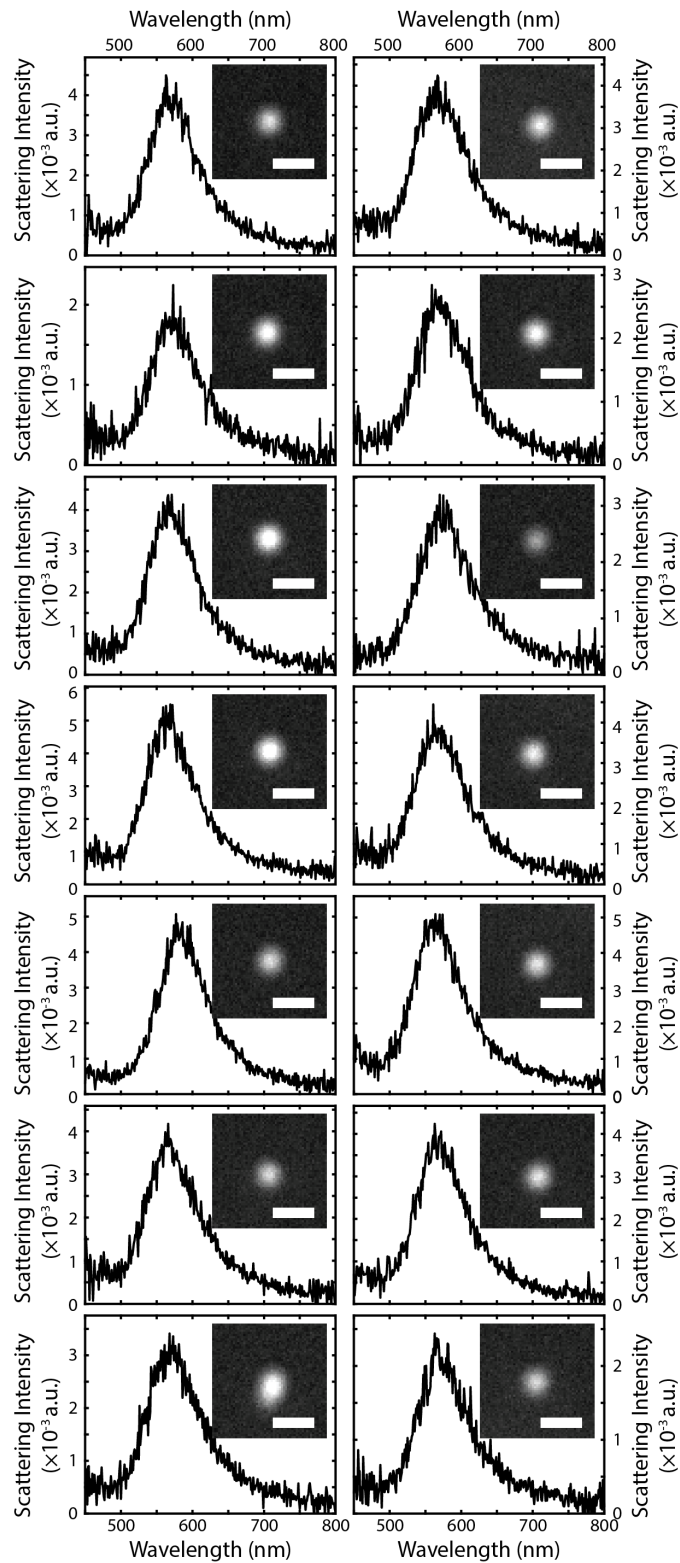
Figure 3.3: Single-particle dark-field spectra of the 14 nanoparticles studied. The normalized spectra were aggregated to produce the grey curve in Figure 3.2. Insets: dark-field scattering images of each particle. Scale bars: 1 μm.
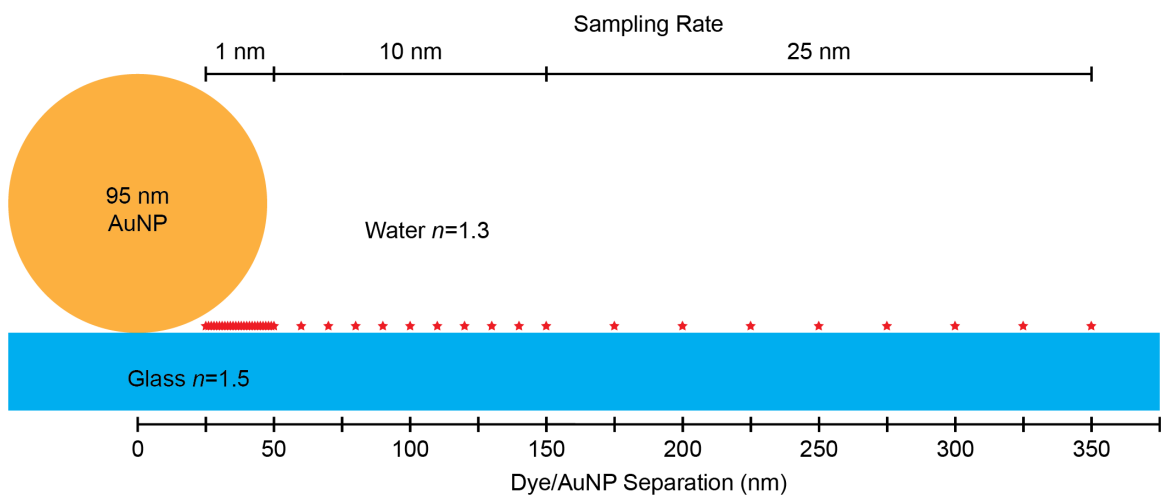
Figure 3.4: Side view of simulated dye positions relative to the positions of the AuNP and glass surface. Point electric dipoles (red stars) were simulated at regular positions, r, according to the sampling rate, next to a gold sphere with a diameter of 95 nm. The read-out of these simulations is described in Figure 3.2b
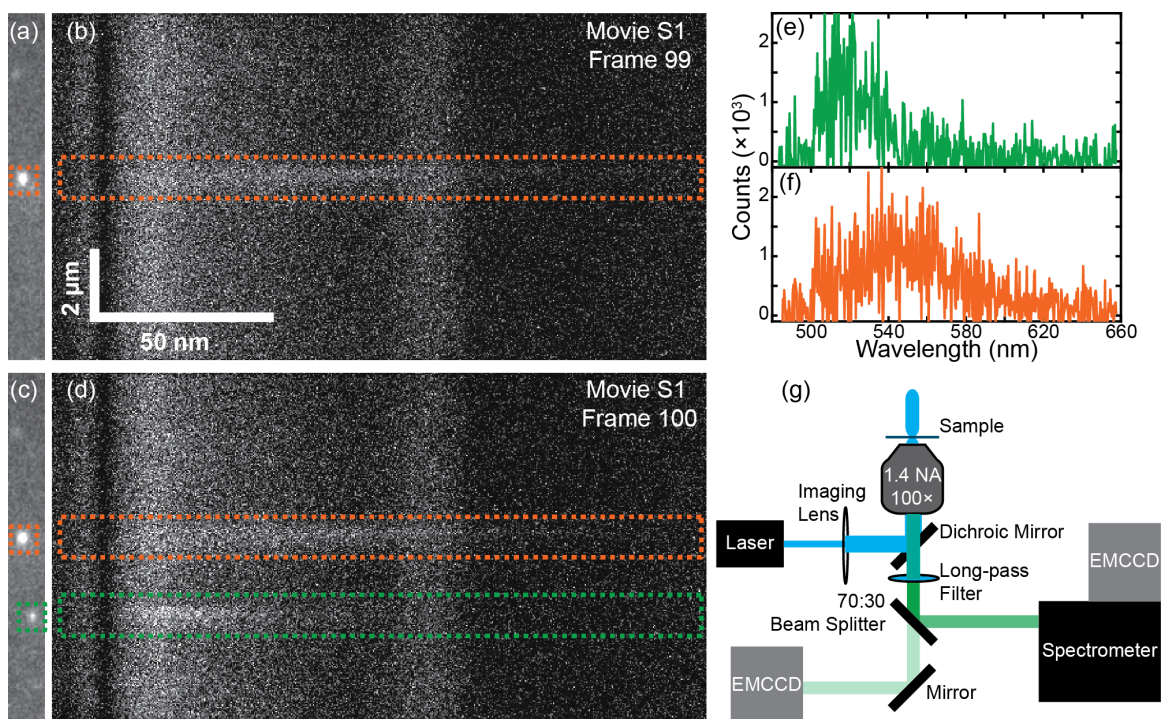
Figure 3.5: (a) Imaging channel with a representative AuNP (orange box). (b) Spectral channel with the corresponding AuNP photoluminescence spectrum. (c) Imaging channel after a BDP-FL dye molecule (green box) adsorbs to the surface several microns from the AuNP (orange box). (d) Spectral channel with corresponding BDP-FL fluorescence and AuNP photoluminescence spectra. (e) Background-subtracted single-molecule fluorescence spectrum of the BDP-FL in the green box in (c,d). (f) Background-subtracted single-particle photoluminescence spectrum of the AuNP in the orange box in (c,d). (g) Single-molecule hyperspectral microscope diagram.

aged and the simulated spectra were similarly binned and averaged for direct comparison (Figure 3.7a,b; Figure 3.8). Because fluorescence emission spectra typically have a peak at the favored vibronic transition wavelength and a redder shoulder that peaks at a longer wavelength, each spectrum was fit with a two-term Gaussian function (Equation 3.4) to evaluate the changes in the emission spectra at each dye/AuNP separation distance.

$$I(\lambda) = I_1\, e^{-\left(\frac{\lambda - \hat{\lambda}_1}{\sigma_1}\right)^2} + I_2\, e^{-\left(\frac{\lambda - \hat{\lambda}_2}{\sigma_2}\right)^2} \tag{3.4}$$

Here, $I(\lambda)$ is the intensity spectrum as a function of wavelength, λ, I_1 and I_2 are the intensities of the main and secondary peaks, respectively, $\hat{\lambda}_1$ and $\hat{\lambda}_2$ are the peak centers in nm, and σ_1 and σ_2 are the peak widths in nm.

The shift in emission maximum, $\Delta\lambda_{max} = \hat{\lambda}'_{max} - \lambda_{max}$, was calculated from the fits to Equation 3.4 for experimental and simulated data (Figure 3.7c and d, respectively). Here, λ_{max} is the main fluorescence emission peak, $\hat{\lambda}_1$ for the uncoupled dye (separation distances greater than 700 nm from a AuNP), and λ'_{max} is the wavelength of whichever peak is brighter for the dye/AuNP coupled system. Thus, $\lambda'_{max} = \hat{\lambda}_1$ when $I_1 \geq I_2$ and $\lambda'_{max} = \hat{\lambda}_2$ when $I_1 < I_2$ (Figure 3.8). In Figure 3.7c,d, $\Delta\lambda_{max}$ is subtle ($|\Delta\lambda_{max}| \lessapprox 5$ nm) for most separation distances but very large for BDP-FL at small separation distances (magenta curve in Figure 3.7c). The source of this large shift is apparent from the bottom-most curves in Figure 3.7a,b: at these small separation distances, the red BDP-FL emission shoulder is much more enhanced than the blue BDP-FL emission peak, and $I_1 < I_2$, giving rise to a > 50 nm spectral emission shift.

To examine the relative enhancement of the emission peak and the emission shoulder, the change in the intensity ratio between the two peaks, $\Delta(I_2/I_1)$, was calculated for each dye/AuNP separation distance in Figure 3.7e,f. Here, $\Delta(I_2/I_1) = I'_2/I'_1 - I_2/I_1$, where I_1 and I_2 are the intensities of the main and secondary peaks in the uncoupled dye and I'_1 and I'_2 are the intensities of the main and secondary peaks in the dye/AuNP coupled system. The emission spectrum reshaping for BDP-FL (Figure 3.7) is maximal for dyes that are very close
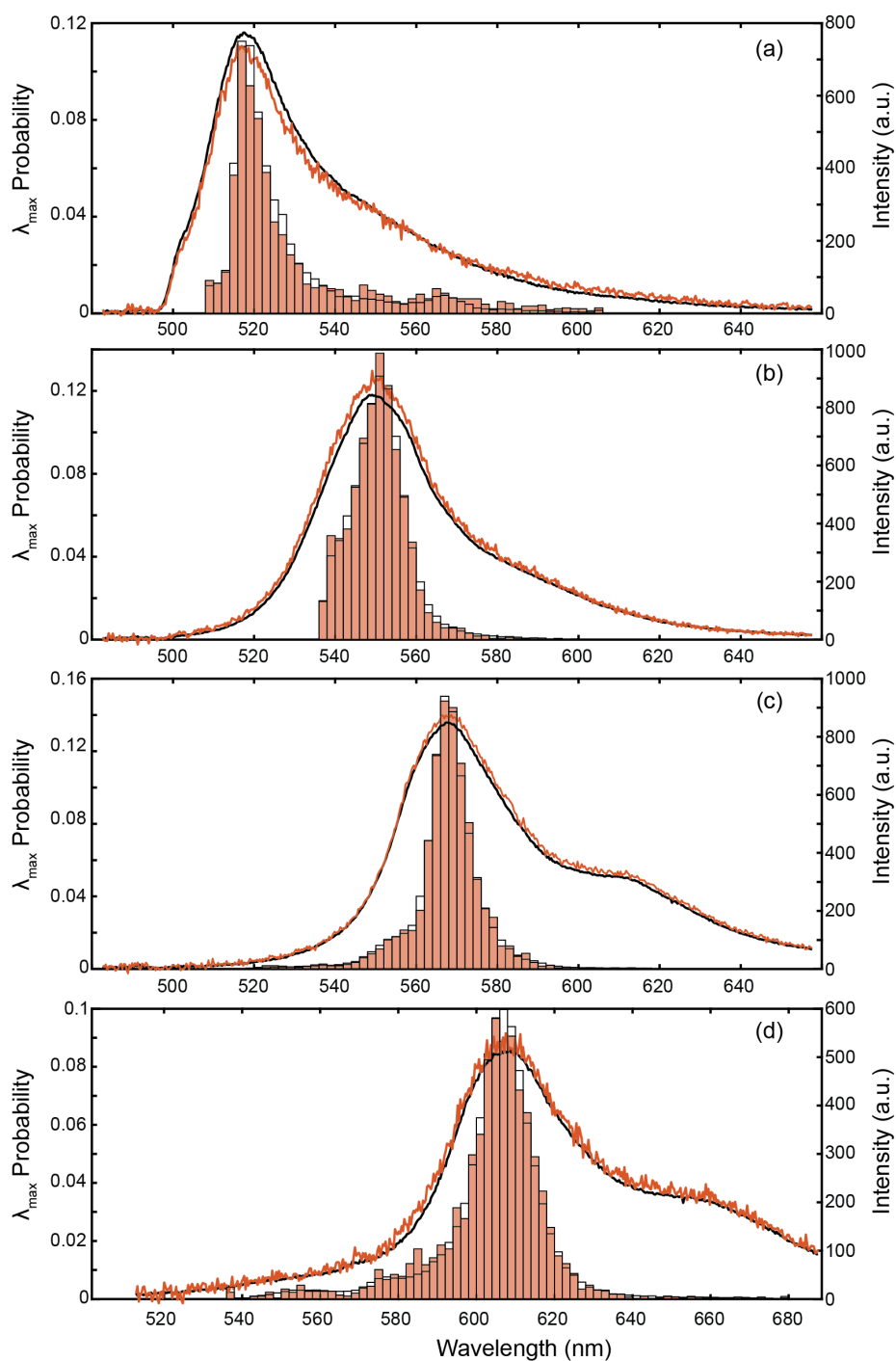
Figure 3.6: Emission maximum distributions (left axis, histograms) and average emission spectra (right axis, curves) for all molecules with *r*>700 nm (blue curve) and *r*<400 nm (orange curve) for each dye: (a) BDP-FL, (b) BDP-R6G, (c) Cy3, and (d) Cy3.5. Here, *r* is the dye/AuNP separation distance (Figure 3.2b).
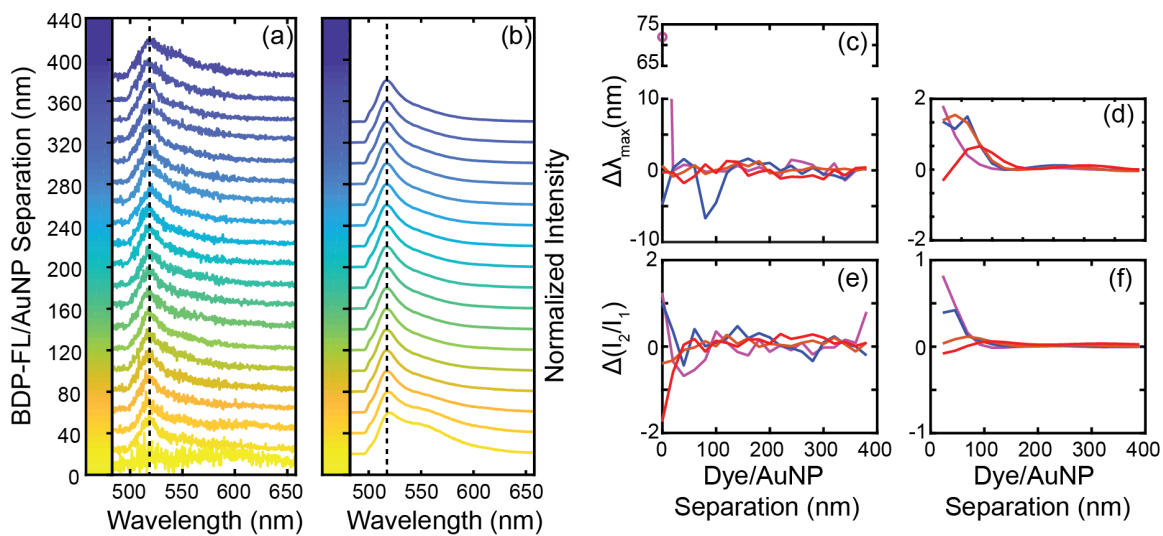
Figure 3.7: (a,b) Average emission spectra for BDP-FL at different dye/AuNP distances for data (a) and simulation (b). Vertical dashed lines represent intrinsic emission maximum. (c,d) Emission maximum change versus dye/nanoparticle separation for (c) data and (d) simulation. (e,f) Change in relative intensity ratio for data (e) and simulation (f). (c–f) BDP-FL, BDP-R6G, Cy3, and Cy3.5 are magenta, blue, orange, and red respectively.
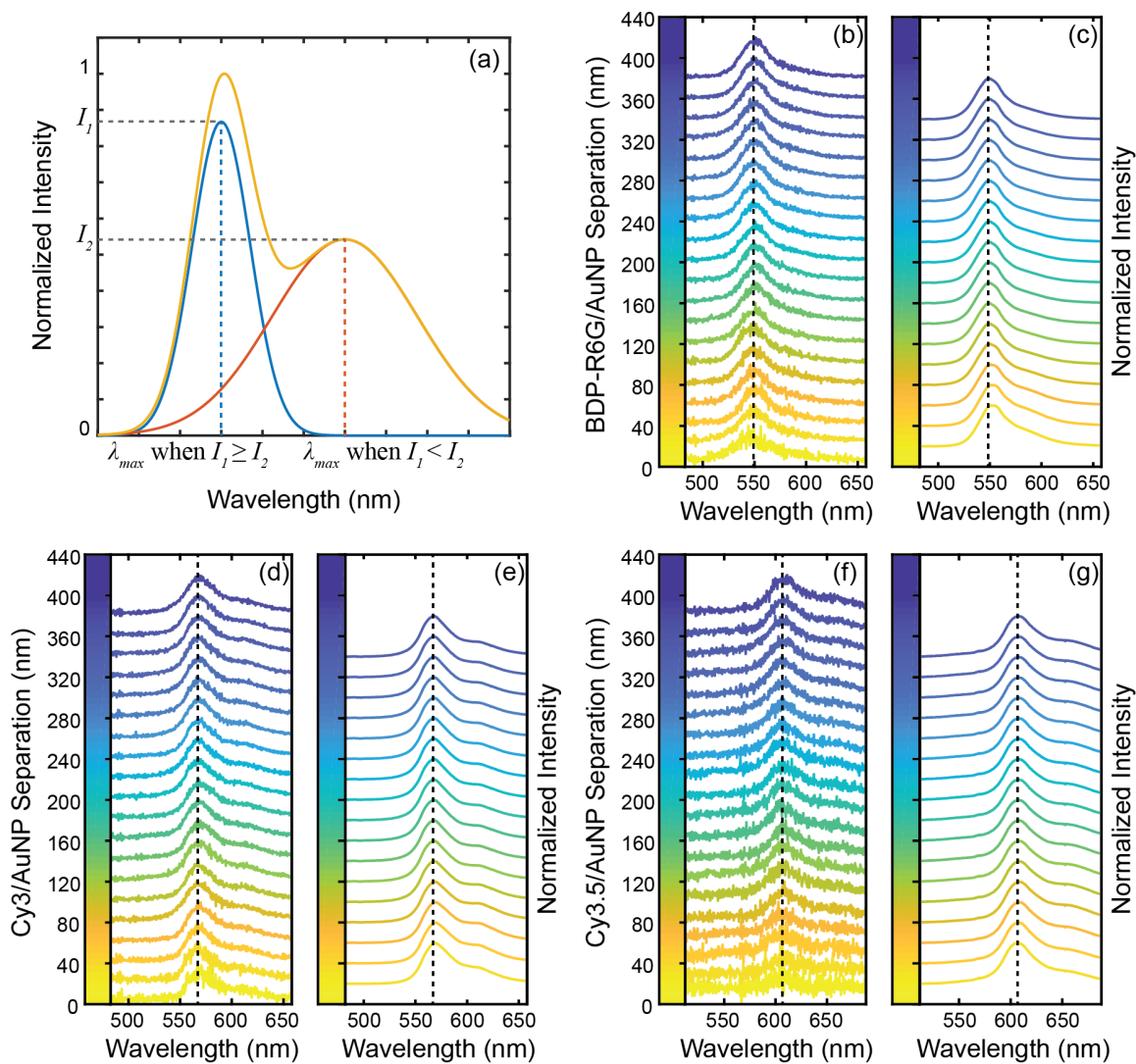
Figure 3.8: (a) Schematic of the two-term Gaussian (Equation 3.4) fit to a single-molecule spectrum. The full fit (yellow curve) is the sum of a Gaussian distribution with intensity I_1 (blue curve) and a Gaussian distribution with intensity I_2 (red curve). The maximum wavelength, λ_{max} is the peak of the blue curve when $I_1 \geq I_2$ (blue dashed line), and the peak of the red curve is λ_{max} when $I_1 < I_2$ (red dashed line). (b–g) Average emission spectra for dyes at different dye/AuNP distances for data (b, d, and f) and simulation (c, e, and g). Vertical dashed lines show the intrinsic emission maximum of each dye.

to the AuNP. Dyes that are localized within 20 nm of the nanoparticle in experiment or 40 nm in simulation show large enhancements of the red shoulder. This asymmetry results in an inversion of the relative intensity of the main and shoulder peaks ($I_2/I_1 > 1$ in Figure 3.7e,f) and leads to a large spectral shift ($\Delta\lambda_{max}$) of greater than 50 nm for experiment, although complete inversions are not seen in the simulated spectra. Shifts in the emission maximum are also seen in BDP-R6G, Cy3, and Cy3.5, but without an inversion of the peak ratios (Figures 3.7c–f and 3.8).

For all the dyes, the changes in the emission spectrum are greatest for separation distances less than 100 nm. The BDP-FL, BDP-R6G, and Cy3 dyes are similar to or bluer than the AuNP LSPR (Figure 3.2a). In these cases, a red shift is observed upon coupling to the plasmonic AuNP: the emission maximum change, $\Delta\lambda_{max}$, and peak intensity ratio change, $\Delta(I_2/I_1)$, are positive, representing an enhancement of the red part of the spectrum over the blue (Figure 3.7c–f). Conversely, Cy3.5, which is redder than the AuNP LSPR (Figure 3.2a), experiences blue shifting: the blue side of the spectrum is more enhanced than the red side.

3.5 Conclusions

Single-molecule hyperspectral imaging allows the measurement of intrinsically hetero-geneous distributions. Emission spectrum reshaping of single molecules coupled to single AuNPs is a distance-dependent process, and simply binning molecules into binary near or far groups obfuscates the more dramatic changes (Figure 3.1). Here, we find that molecules localized within 100 nm of the AuNPs experience the greatest changes in their spectrum and we measure an overall trend: dyes with emission bluer than the LSPR experience a red-shifting of the emission spectrum and dyes with emission redder than the LSPR will experience a blue-shifting of the emission spectrum. Plasmon-enhanced fluorescence is a resonant process, which leads to selective enhancement of one vibronic transition over another; this coupling produces spectral reshaping. The extent of spectral reshaping overall

agrees with electromagnetic simulations. Here, we have not accounted for mislocalization of the molecules, where the apparent position of a molecule is shifted from the actual position due to coupling with the nanoparticle [32, 33, 39, 86]. Thus, we attribute the differences between experimental results and simulation primarily to the mislocalization effect. These results demonstrate the power of single-molecule hyperspectral imaging. We believe that these results may also be used in conjunction with analytical models of plasmon/dye coupling to recover the actual position of a fluorophore in a coupled system [86].

CHAPTER IV

Conclusions and Future Directions

4.1 Conclusions

Single-molecule and single-particle imaging is an indispensable tool for studying the heterogeneity of nano- and microscopic systems. In Chapter II, the single-molecule technique, photoactivated localization microscopy (PALM) was used to evaluate the enhancement of fluorescent proteins in living *V. cholerae* cells on nanosphere lithography (NSL)-fabricated nanotriangle arrays (NTAs), uncovering some trade-offs between nanoparticle (NP) size and array coverage when using NSL for array fabrication, revealing greatest enhancement not for the best resonance overlap, but for the optimal combination of surface coverage and overlap. We also expanded on the findings from Chapter II and examined a much wider parameter space for enhanced, live-cell imaging using electron-beam lithography (EBL) fabricated nanoparticle arrays (NPAs) in Chapter II. Additionally, in Chapter III, hyperspectral points accumulation for imaging in nanoscale topography (PAINT) was used to study the distance- and wavelength-dependent coupling of individual dyes with single gold nanoparticles (AuNPs). There, the emission spectrum reshaping of four different fluorophores were characterized and the distance dependent spectral reshaping was thoroughly analyzed, revealing that dyes redder than the localized surface plasmon resonance (LSPR) were blue-shifted, and dyes bluewer than the LSPR were red-shifted. In addition to PALM and PAINT, dark-field imaging was used to measure the

LSPR modes of the arrays and individual particles, enabling evaluation of the heterogeneity of the particles.

4.2 Future Applications and Technologies

4.2.1 Gold nanoparticles as absolute nanothermometers

Gold nanoparticles have interested scientists for over 150 years, since Michael Faraday first described optical scattering of gold nanoparticles as the cause of the ruby tint in colloidal gold solutions [87]. Although there has been a wealth of research on the scattering and enhancement properties of gold nanoparticles [88, 89], they also exhibit absorption and photoluminescence [90–92]. Although the mechanism of gold photoluminescence is hotly debated [91, 92], it has nevertheless been useful in single-molecule and single-particle imaging: plasmonic nanoparticles have been used as a fiduciary for drift correction and super-localization [28, 93]. In addition to emitting, an absorbed photon can also be converted to local heat, which is the principle behind photothermal therapy and photothermal imaging with gold nanoparticles [94–97]. The temperature gradients produced by gold nanoparticle photothermal conversion can be quite intense [98], but many methods for measuring the temperature are in bulk and performed in the steady-state [99, 100]. Recently, a new method of nanothermometry was developed that uses the intrinsic photoluminescence of gold as a readout for the local temperature and nanoparticle temperature [101]. This method uses the photoluminescence spectrum of a gold nanoparticle excited above the LSPR band, and the antistokes emission spectrum from on-resonance excitation to extract the temperature of the nanoparticle and the surrounding medium. We build on these principles and propose an all-fluorescence method for AuNP nanothermometry requiring only the photoluminescence intensity of a AuNP.

4.2.1.1   Sample preparation and gold nanoparticle characterization

Nominally 80-nm AuNPs (BBI solutions) were drop-cast onto a labeled grid coverslip and dried under nitrogen. The AuNPs were imaged in a dark-field spectroscopy (DFS) setup where an oil immersed dark-field condenser (1.2–1.4 numerical aperture (NA)) was used to focus the light from a halogen lamp onto the sample. The light scattered from the sample was collected through a 100× 0.6 NA oil immersion objective. A region of single AuNPs was found, and each particle's DFS spectrum was recorded (Figure 4.1).

4.2.1.2   Single-particle nanothermometry

The photoluminescence intensity of each particle was recorded at various temperatures between 26 and 56 ^{o}C and various 561-nm laser excitation powers between 5 and 50 W·cm^{-1}. The microscope was fitted with an objective heater with feedback control to maintain the temperature of an oil thermal bath, a thermocouple was placed into the thermal bath for continuous temperature monitoring, and automated stage and focus control were used to compensate for thermal drift (Figure 4.2). The photoluminescence was collected through a 1.4 NA objective and the elastic scatter was filtered by a 561-nm dichroic and long-pass filter set (Semrock Di01-R561 and BLP01-561). The photoluminescence image was collected on an electron multiplying charge-coupled device (EMCCD) camera (Andor iXon 897) with 100-ms exposure time. Each image sequence was taken at a particular temperature (26–56 ^{o}C nominal temperature) and nominal laser power (5–50 mW output). For each frame, the bath temperature was recorded and the power delivered to each particle was calculated based on the illumination profile in the image.

4.2.1.3   Preliminary Results

The single-particle positions and intensities were determined by subtracting the fitted background from each image and using the SMALL-LABS program to find and fit each particle in the image [85]. The particle positions were then used to determine the actual
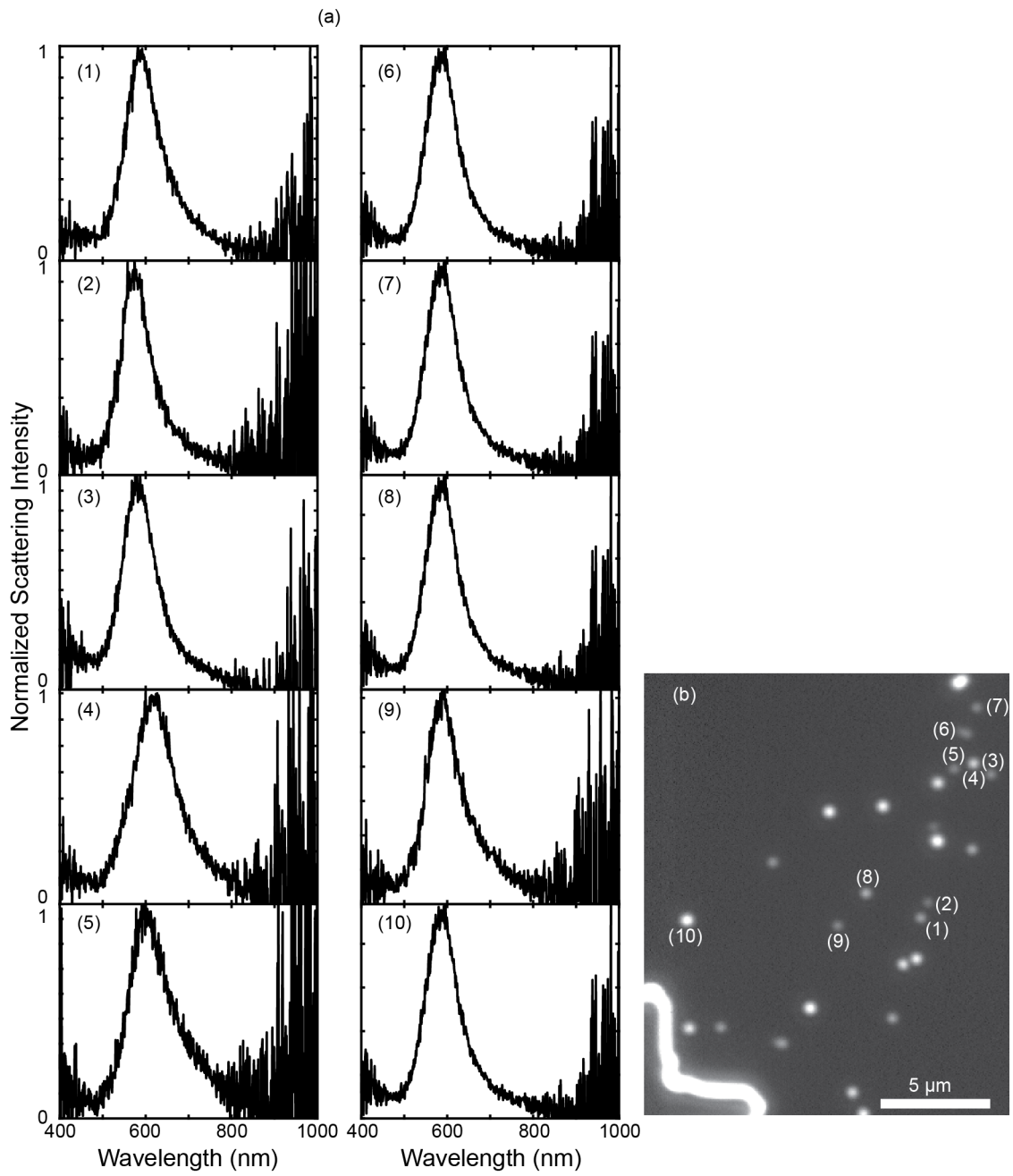
Figure 4.1: (a) Single-particle DFS spectra. (b) Nanoparticle locations for each spectrum in (a).
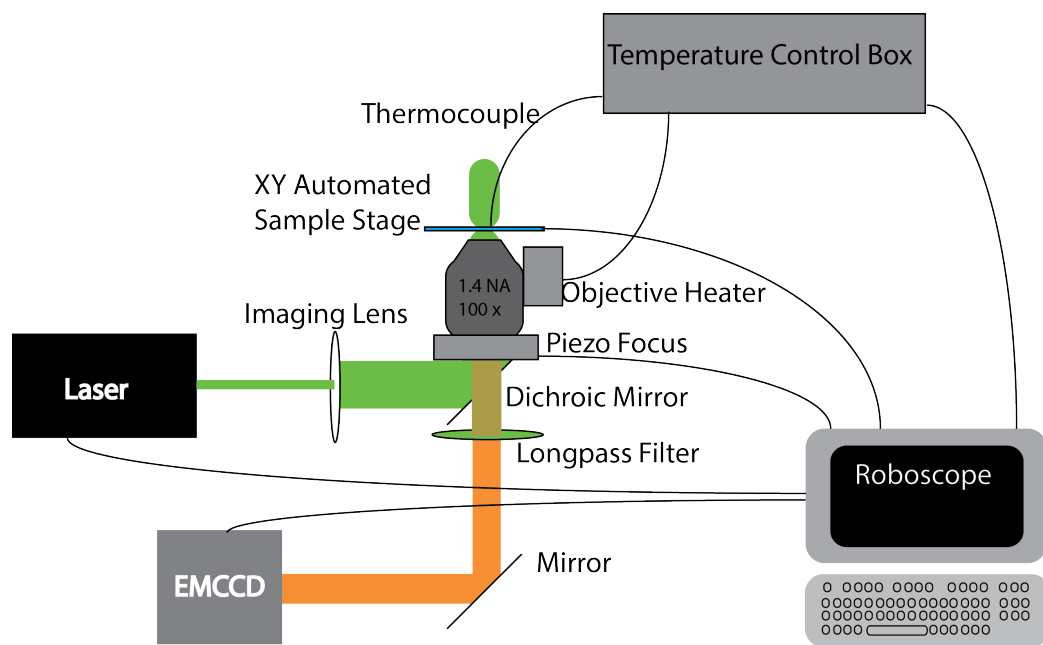
Figure 4.2: Single-particle nanothermometry microscope setup.

power delivered to the particle at each temperature within the Gaussian illumination spot. Particles with the same illumination power and temperature were averaged together to obtain the emission intensity at that particular power and temperature combination (Figure 4.3).

As seen in Figure 4.3, the photoluminescence intensity decreases with increasing temperature, and increases with increasing power. The results are qualitatively consistent with the theory presented in [101], where the increase in temperature leads to an increase in the phonon occupation number, $\bar{n}$ (Equation 4.1).

$$\bar{n} = \left(\exp \frac{\hbar \Omega}{k_B T} - 1 \right)^{-1} \tag{4.1}$$

where $\hbar\Omega$ is the phonon energy and $k_B T$ is the thermal energy.

The increase in phonon occupation number leads to a decrease in Stokes photoluminescence intensity, Ω, Equation 4.2.

$$I(\omega) = I_{LSPR}(\omega) \left(\left(\exp \frac{\hbar(\omega - \omega_L)}{k_B T} - 1 \right)^{-1} + 1 \right) \tag{4.2}$$

where $I(\omega)$ is the emission intensity at frequency ω and ω_L is the laser frequency.

4.2.1.4   Conclusions

Although there is a clear non-linear dependence of the photoluminescence on the excitation power and bath temperature, the next steps for determining the temperature of the nanoparticle are not clear, given the lack of spectral information from this particular experiment. Two possible paths to proceed along are to use a particular slice of the data as the baseline and establish a calibration curve, or to perform the experiment with hyperspectral imaging (Chapter III to obtain the emission spectrum as well. Additionally, the theoretical method described in [101] assumes that the photoluminescence is dominated by phonon coupling, but other theoretical frameworks propose that carrier-carrier interactions domi-
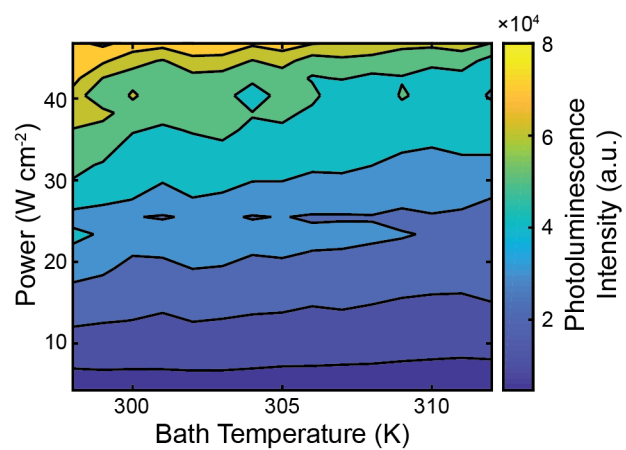
Figure 4.3: Contour map of the AuNP photoluminescence intensity at different 561-nm laser powers and bath temperatures.

nate and would obey Fermi statistics [91, 102]. Thus, in addition to identifying a method to extract the thermal information for these results, a more comprehensive understanding of the origin of photoluminescence emission is necessary to justify that the method is actually measuring the temperature of the particle and not the thermal distribution of hot electron/hole pairs.

4.2.2 Advances in live-cell imaging

Overall, plasmonics stands to fundamentally improve super-resolution imaging by addressing single-molecule fluorescence limitations, such as low brightness, through excitation confinement, enhanced electric field intensities, and increased local density of states. Looking forward, plasmonics will allow a variety of spectroscopies, including fluorescence and Raman, to be performed on the subcellular level to obtain dynamic chemical and structural information. Additionally, plasmonic nanoparticle arrays will improve the resolution of fluorescence microscopy to the order of the size of the emitter and reduce photobleaching for monitoring real-time protein dynamics [28]. For instance, we envision combining plasmonics and nanofluidics to produce a platform for confined, physiological, enhanced imaging in bacteria (Figure 4.4). Overall, as technologies improve, all of the tools discussed here can be combined to reach higher levels of understanding about fundamental, subcellular biology. Through innovative combinations of confinement approaches, imaging modalities, and nanotechnologies, we will finally close the mismatch between the spatial resolution of light microscopy and the nanoscale world of cellular biophysics to enable a wealth of discoveries [45].

4.2.3 Advances in single-molecule information content

There is a wealth of information stored in each molecules emission; the fluorescence position, polarization, and spectrum each encode information about the molecule and its local environment. There are many methods to get at one or two of these properties (see
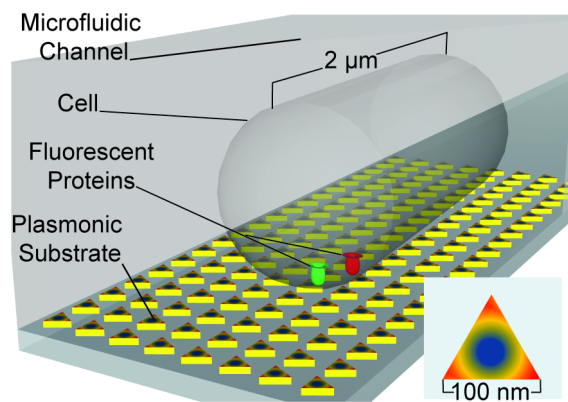
Figure 4.4: Single-cell analysis on a plasmonic substrate within a microfluidic channel will permit active control of the cellular environment. Two intracellular fluorescent proteins (red and green) couple to the plasmonic substrate for plasmon-enhanced two-color single-molecule imaging. (Inset) Electric field enhancement above each plasmonic nanotriangle [45].

references [83, 103, 104] and Chapter III), but very few to measure all three simultaneously [105].

Here, I propose a new method for obtaining single-molecule or single-particle, hyperspectral, polarization images (Figure 4.5). The microscope setup involves two channels separated by a beamsplitter and made orthogonal in the image-plane polarization by placing a half-wave plate in one of the paths. Each channel is then split with a wavelength-dependent, polarizing beam displacer (PBD) into relative parallel (P∥) and perpendicular (P⊥) polarized channels imaged on an EMCCD camera. The image-space relative polarizations of the molecules are obtained according to Equation 4.3, and the spectrum is acquired from the wavelength-dependent displacement in the P⊥ channels.

$$\theta = \arctan\left(\sqrt{\frac{I_\parallel}{I_\perp}}\right) \tag{4.3}$$

where θ is the relative angle of the molecule in the image plane, $I_\parallel$ is the intensity of the molecule image in the P∥ channel, and $I_\perp$ is the intensity of the molecule image in the P⊥ channel.

Even though the spectrum and polarization can be obtained with only one channel, if the relative orientation of the object is aligned in either of the P∥ or P⊥ channels, either the localization or spectrum is lost since all of the signal will be in the orthogonal channel. If the signal is only in the displaced channel (P⊥), only a spectrum can be obtained due to the missing correlated image in the P∥ channel. Conversely, if the signal is only in the P∥ channel, only a localization can be obtained due to the missing correlated image in the P⊥ channel. By splitting the signal into two orthogonal channels, the aligned molecule/particle can contain both localization and spectral components as well as two measures of the image-plane orientation. Thus the information quality and content is improved.

Applications for this hyperspectral, polarization, super-resolution imaging method are numerous. When fluorescent molecules couple with a plasmonic nanoparticle, the emission is no longer from the fluorophore alone, but from the coupled system, which
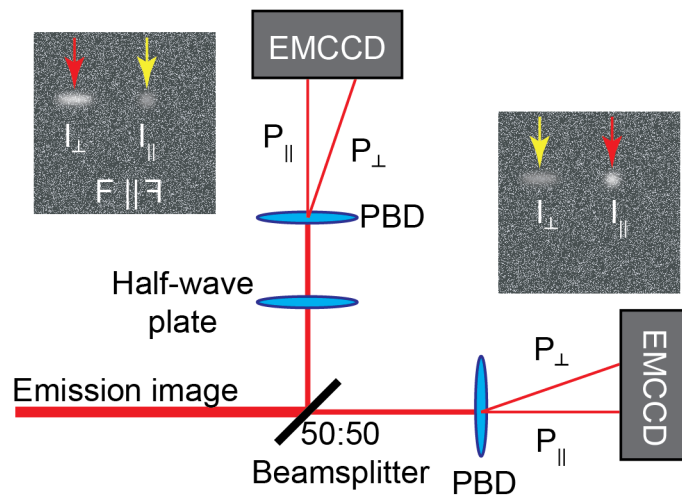
Figure 4.5: Hyperspectral polarization imaging setup. red and yellow arrows indicate same polarization component in the imaging plane. The image in the reflected channel is mirror-transformed to match the transmitted channel.

results in a point-spread function that when fit with a 2-D Gaussian function gives the wrong position, this effect is known as mislocalization. Having both spectral and polarization information will advance solving the mislocalization problem that occurs when emitters couple with plasmonic nanoparticles by providing more information about the coupling to be used with analytic models of emitter/nanoparticle coupling [32, 33, 39, 86]. Hyperspectral-anisotropy, super-resolution imaging could allow for studying biological systems with multiple different fluorophores targeted to cellular regions of differing viscosity or organization. The fluorophores could be separated by emission spectrum and the local viscosity or organization can be measured by the molecule orientations [106].

Super-resolution fluorescence imaging has proved an invaluable tool in studying light-matter interactions and dynamics in live-cell imaging. Further methods and technological advances within the field ensure that super-resolution fluorescence imaging will continue to be at the forefront of uncovering the mysteries of the nanoscopic world.

BIBLIOGRAPHY

BIBLIOGRAPHY

[1] A. J. M. Wollman, R. Nudd, E. G. Hedlund, M. C. Leake, "From animaculum to single molecules: 300 years of the light microscope", *Open Biology* **5**, 150019. DOI: 10.1098/rsob.150019.

[2] E. Abbe, "Beiträge zur theorie des mikroskops und der mikroskopischen wahrnehmung", *Archiv für Mikroskopische Anatomie* **9**, 413. DOI: 10.1007/BF02956173.

[3] N. Liv, *et al.*, "Electron microscopy of living cells during in situ fluorescence microscopy", *ACS Nano* **10**, 265. DOI: 10.1021/acsnano.5b03970.

[4] Y. Wu, G. Li, J. P. Camden, "Probing nanoparticle plasmons with electron energy loss spectroscopy", *Chemical Reviews* **118**, 2994. DOI: 10.1021/acs.chemrev.7b00354.

[5] W. E. Moerner, L. Kador, "Optical detection and spectroscopy of single molecules in a solid", *Physical Review Letters* **62**, 2535. DOI: 10.1103/PhysRevLett.62.2535.

[6] E. Brooks Shera, N. K. Seitzinger, L. M. Davis, R. A. Keller, S. A. Soper, "Detection of single fluorescent molecules", *Chemical Physics Letters* **174**, 553. DOI: 10.1016/0009-2614(90)85485-U.

[7] T. Funatsu, Y. Harada, M. Tokunaga, K. Saito, T. Yanagida, "Imaging of single fluorescent molecules and individual ATP turnovers by single myosin molecules in aqueous solution", *Nature* **374**, 555. DOI: 10.1038/374555a0.

[8] B. Huang, M. Bates, X. Zhuang, "Super-resolution fluorescence microscopy", *Annual Review of Biochemistry* **78**, 993. DOI: 10.1146/annurev.biochem.77.061906.092014.

[9] M. A. Thompson, M. D. Lew, W. Moerner, "Extending microscopic resolution with single-molecule imaging and active control", *Annual Review of Biophysics* **41**, 321. DOI: 10.1146/annurev-biophys-050511-102250.

[10] K. A. Willets, A. J. Wilson, V. Sundaresan, P. B. Joshi, "Super-resolution imaging and plasmonics", *Chemical reviews* **117**, 7538.

[11] S. T. Hess, T. P. Girirajan, M. D. Mason, "Ultra-high resolution imaging by fluorescence photoactivation localization microscopy", *Biophysical Journal* **91**, 4258. DOI: 10.1529/biophysj.106.091116.

[12] A. Sharonov, R. M. Hochstrasser, "Wide-field subdiffraction imaging by accumulated binding of diffusing probes", *Proceedings of the National Academy of Sciences* **103**, 18911. DOI: 10.1073/pnas.0609643104.

[13] C. L. Haynes, A. D. McFarland, R. P. V. Duyne, "Surface-enhanced raman spectroscopy", *Analytical Chemistry* **77**, 338 A. DOI: 10.1021/ac053456d.

[14] E. Cortés, *et al.*, "Plasmonic hot electron transport drives nano-localized chemistry", *Nature Communications* **8**, 14880. DOI: 10.1038/ncomms14880.

[15] M. T. Sheldon, J. V. De Groep, A. M. Brown, A. Polman, H. A. Atwater, "Plasmoelectric potentials in metal nanostructures", *Science* **346**, 828. DOI: 10.1126/science.1258405.

[16] P. M. R. Paulo, *et al.*, "Photothermal correlation spectroscopy of gold nanoparticles in solution", *Journal of Physical Chemistry C* **113**, 11451. DOI: 10.1021/jp806875s.

[17] L. Novotny, N. v. Hulst, "Antennas for light", *Nature Photonics* **5**, 83.

[18] S. Link, M. A. El-Sayed, "Shape and size dependence of radiative, non-radiative and photothermal properties of gold nanocrystals", *International Reviews in Physical Chemistry* **19**, 409. DOI: 10.1080/01442350050034180.

[19] C. J. Murphy, *et al.*, "Anisotropic metal nanoparticles: Synthesis, assembly, and optical applications", *Journal of Physical Chemistry B* **109**, 13857. DOI: 10.1021/jp0516846.

[20] K. A. Willets, R. P. Van Duyne, "Localized surface plasmon resonance spectroscopy and sensing", *Annual Review of Physical Chemistry* **58**, 267. DOI: 10.1146/annurev.physchem.58.032806.104607.

[21] S. A. Maier, H. A. Atwater, "Plasmonics: Localization and guiding of electromagnetic energy in metal/dielectric structures", *Journal of Applied Physics* **98**, 011101. DOI: 10.1063/1.1951057.

[22] S. Eustis, M. A. El-Sayed, "Why gold nanoparticles are more precious than pretty gold: Noble metal surface plasmon resonance and its enhancement of the radiative and nonradiative properties of nanocrystals of different shapes", *Chem. Soc. Rev.* **35**, 209. DOI: 10.1039/B514191E.

[23] R. Zhang, *et al.*, "How to identify plasmons from the optical response of nanostructures", *ACS Nano* **11**, 7321. DOI: 10.1021/acsnano.7b03421.

[24] R. E. Thompson, D. R. Larson, W. W. Webb, "Precise nanometer localization analysis for individual fluorescent probes", *Biophysical Journal* **82**, 2775. DOI: 10.1016/S0006-3495(02)75618-X.

[25] P. Anger, P. Bharadwaj, L. Novotny, "Enhancement and quenching of single-molecule fluorescence", *Physical Review Letters* **96**, 113002.

[26] S. Bharill, *et al.*, "Enhancement of single-molecule fluorescence signals by colloidal silver nanoparticles in studies of protein translation", *ACS Nano* **5**, 399.

[27] H. Yuan, S. Khatua, P. Zijlstra, M. Yorulmaz, M. Orrit, "Thousand-fold enhancement of single-molecule fluorescence near a single gold nanorod", *Angewandte Chemie - International Edition* **52**, 1217. DOI: 10.1002/anie.201208125.

[28] J. E. Donehue, E. Wertz, C. N. Talicska, J. S. Biteen, "Plasmon-enhanced brightness and photostability from single fluorescent proteins coupled to gold nanorods", *Journal of Physical Chemistry C* **118**, 15027. DOI: 10.1021/jp504186n.

[29] B. Fu, B. P. Isaacoff, J. S. Biteen, "Super-resolving the actual position of single fluorescent molecules coupled to a plasmonic nanoantenna", *ACS Nano* **11**, 8978. DOI: 10.1021/acsnano.7b03420.

[30] S. A. Lee, J. S. Biteen, "Interplay of nanoparticle resonance frequency and array surface coverage in live-cell plasmon-enhanced single-molecule imaging", *The Journal of Physical Chemistry C* **122**, 5705. DOI: 10.1021/acs.jpcc.8b01436.

[31] E. A. Wertz, B. P. Isaacoff, J. S. Biteen, "Wavelength-dependent super-resolution images of dye molecules coupled to plasmonic nanotriangles", *ACS Photonics* **3**, 1733. DOI: 10.1021/acsphotonics.6b00344.

[32] K. L. Blythe, E. J. Titus, K. A. Willets, "Comparing the accuracy of reconstructed image size in super-resolution imaging of fluorophore-labeled gold nanorods using different fit models", *The Journal of Physical Chemistry C* **119**, 19333. DOI: 10.1021/acs.jpcc.5b04993.

[33] K. Lim, *et al.*, "Nanostructure-induced distortion in single-emitter microscopy", *Nano Letters* **16**, 5415. DOI: 10.1021/acs.nanolett.6b01708.

[34] S. Siavoshi, *et al.*, "Size-selective template-assisted electrophoretic assembly of nanoparticles for biosensing applications", *Langmuir* **27**, 7301. DOI: 10.1021/la104975u.

[35] H. Zhang, *et al.*, "Direct assembly of large area nanoparticle arrays", *ACS Nano* **12**, 7529. DOI: 10.1021/acsnano.8b02932.

[36] M. Li, *et al.*, "Bottom-up assembly of large-area nanowire resonator arrays", *Nature Nanotechnology* **3**, 88. DOI: 10.1038/nnano.2008.26.

[37] L. Lin, *et al.*, "Bubble-pen lithography", *Nano Letters* **16**, 701. DOI: 10.1021/acs.nanolett.5b04524.

[38] J. Gargiulo, *et al.*, "Accuracy and mechanistic details of optical printing of single au and ag nanoparticles", *ACS Nano* **11**, 9678. DOI: 10.1021/acsnano.7b04136.

[39] E. Wertz, B. P. Isaacoff, J. D. Flynn, J. S. Biteen, "Single-molecule super-resolution microscopy reveals how light couples to a plasmonic nanoantenna on the nanometer scale", *Nano Letters* **15**, 2662. DOI: 10.1021/acs.nanolett.5b00319.

[40] V. Flauraud, *et al.*, "Large-scale arrays of bowtie nanoaperture antennas for nanoscale dynamics in living cell membranes", *Nano Letters* **15**, 4176. DOI: 10.1021/acs.nanolett.5b01335.

[41] C. L. Haynes, R. P. Van Duyne, "Nanosphere lithography: A versatile nanofabrication tool for studies of size-dependent nanoparticle optics", *The Journal of Physical Chemistry B* **105**, 5599. DOI: 10.1021/jp010657m.

[42] E. Betzig, *et al.*, "Imaging intracellular fluorescent proteins at nanometer resolution", *Science* **313**, 1642. DOI: 10.1126/science.1127344.

[43] M. J. Rust, M. Bates, X. Zhuang, "Sub-diffraction-limit imaging by stochastic optical reconstruction microscopy (STORM)", *Nature Methods* **3**, 793. DOI: 10.1038/nmeth929.

[44] S. W. Hell, "Far-field optical nanoscopy", *Science* **316**, 1153. DOI: 10.1126/science.1137395.

[45] S. A. Lee, A. Ponjavic, C. Siv, S. F. Lee, J. S. Biteen, "Nanoscopic cellular imaging: Confinement broadens understanding", *ACS Nano* **10**, 8143. DOI: 10.1021/acsnano.6b02863 [doi].

[46] K. L. Blythe, K. A. Willets, "Super-resolution imaging of fluorophore-labeled DNA bound to gold nanoparticles: A single-molecule, single-particle approach", *Journal of Physical Chemistry C* **120**, 803. DOI: 10.1021/acs.jpcc.5b08534.

[47] M. Raab, C. Vietz, F. D. Stefani, G. P. Acuna, P. Tinnefeld, "Shifting molecular localization by plasmonic coupling in a single-molecule mirage", *Nature Communications* **8**, 13966.

[48] G. C. H. Mo, *et al.*, "Genetically encoded biosensors for visualizing live-cell biochemical activity at super-resolution", *Nature Methods* **14**, 427.

[49] Y. Liao, Y. Li, J. W. Schroeder, L. A. Simmons, J. S. Biteen, "Single-molecule DNA polymerase dynamics at a bacterial replisome in live cells", *Biophysical Journal* **111**, 2562. DOI: 10.1016/j.bpj.2016.11.006.

[50] T. R. Beattie, *et al.*, "Frequent exchange of the DNA polymerase during bacterial chromosome replication", *eLife* **6**, 10.7554. DOI: 10.7554/eLife.21763 [doi].

[51] J. S. Lewis, *et al.*, "Single-molecule visualization of fast polymerase turnover in the bacterial replisome", *eLife* **6**, e23932. DOI: 10.7554/eLife.23932.

[52] A. Yildiz, *et al.*, "Myosin v walks hand-over-hand: Single fluorophore imaging with 1.5-nm localization", *Science* **300**, 2061.

[53] D. A. Yushchenko, M. P. Bruchez, *Far-Field Optical Nanoscopy*, P. Tinnefeld, C. Eggeling, S. W. Hell, eds., Springer Series on Fluorescence (Springer Berlin Heidelberg), pp. 159–188.

[54] G. Zhang, V. Gurtu, S. R. Kain, "An enhanced green fluorescent protein allows sensitive detection of gene transfer in mammalian cells", *Biochemical and Biophysical Research Communications* **227**, 707. DOI: 10.1006/bbrc.1996.1573.

[55] N. Mataga, Y. Kaifu, M. Koizumi, "Solvent effects upon fluorescence spectra and the dipolemoments of excited molecules", *Bulletin of the Chemical Society of Japan* **29**, 465. DOI: 10.1246/bcsj.29.465.

[56] J.-F. Li, C.-Y. Li, R. F. Aroca, "Plasmon-enhanced fluorescence spectroscopy", *Chemical Society Reviews* **46**, 3962. DOI: 10.1039/C7CS00169J.

[57] A. Rose, *et al.*, "Control of radiative processes using tunable plasmonic nanopatch antennas", *Nano Letters* **14**, 4797. DOI: 10.1021/nl501976f.

[58] G. M. Akselrod, *et al.*, "Probing the mechanisms of large purcell enhancement in plasmonic nanoantennas", *Nature Photonics* **8**, 835. DOI: 10.1038/nphoton.2014.228.

[59] N. S. Abadeer, M. R. Brennan, W. L. Wilson, C. J. Murphy, "Distance and plasmon wavelength dependent fluorescence of molecules bound to silica-coated gold nanorods", *ACS Nano* **8**, 8392. DOI: 10.1021/nn502887j.

[60] J. R. Lakowicz, *et al.*, "Radiative decay engineering", *Analytical Biochemistry* **301**, 261. DOI: 10.1006/abio.2001.5503.

[61] C. Ropp, *et al.*, "Nanoscale probing of image-dipole interactions in a metallic nanostructure", *Nature Communications* **6**, 6558. DOI: 10.1038/ncomms7558.

[62] J. D. Flynn, B. L. Haas, J. S. Biteen, "Plasmon-enhanced fluorescence from single proteins in living bacteria", *Journal of Physical Chemistry C* **120**, 20512. DOI: 10.1021/acs.jpcc.5b08049.

[63] J. C. Hulteen, R. P. V. Duyne, "Nanosphere lithography: A materials general fabrication process for periodic particle array surfaces", *Journal of Vacuum Science & Technology A: Vacuum, Surfaces, and Films* **13**, 1553.

[64] S. Link, M. B. Mohamed, M. A. El-Sayed, "Simulation of the optical absorption spectra of gold nanorods as a function of their aspect ratio and the effect of the medium dielectric constant", *The Journal of Physical Chemistry B* **103**, 3073. DOI: 10.1021/jp990183f.

[65] J. S. Matson, J. H. Withey, V. J. DiRita, "Regulatory networks controlling vibrio cholerae virulence gene expression", *Infection and immunity* **75**, 5542. DOI: 10.1128/IAI.01094-07.

[66] B. L. Haas, J. S. Matson, V. J. DiRita, J. S. Biteen, "Single-molecule tracking in live vibrio cholerae reveals that ToxR recruits the membrane-bound virulence regulator TcpP to the toxT promoter", *Molecular Microbiology* **96**, 4. DOI: 10.1111/mmi.12834.

[67] F. V. Subach, *et al.*, "Photoactivatable mCherry for high-resolution two-color fluorescence microscopy", *Nature Methods* **6**, 153.

[68] B. Fu, J. D. Flynn, B. P. Isaacoff, D. J. Rowland, J. S. Biteen, "Super-resolving the distance-dependent plasmon-enhanced fluorescence of single dye and fluorescent protein molecules", *Journal of Physical Chemistry C* **119**, 19350. DOI: 10.1021/acs.jpcc.5b05154.

[69] Y. Chen, K. Munechika, D. Ginger, "Dependence of fluorescence intensity on the spectral overlap between fluorophores and plasmon resonant single silver nanoparticles", *Nano Lett.* **7**, 690.

[70] O. Stranik, R. Nooney, C. McDonagh, B. D. MacCraith, "Optimization of nanoparticle size for plasmonic enhancement of fluorescence", *Plasmonics* **2**, 15. DOI: 10.1007/s11468-006-9020-9.

[71] G. H. Patterson, J. Lippincott-Schwartz, "A photoactivatable GFP for selective photolabeling of proteins and cells", *Science* **297**, 1873.

[72] Y. Liao, J. W. Schroeder, B. Gao, L. A. Simmons, J. S. Biteen, "Single-molecule motions and interactions in live cells reveal target search dynamics in mismatch repair", *Proceedings of the National Academy of Sciences* **112**, E6898. DOI: 10.1073/pnas.1507386112.

[73] V. G. Kravets, A. V. Kabashin, W. L. Barnes, A. N. Grigorenko, "Plasmonic surface lattice resonances: A review of properties and applications", *Chemical Reviews* **118**, 5912. DOI: 10.1021/acs.chemrev.8b00243.

[74] A. Egner, *et al.*, "Fluorescence nanoscopy in whole cells by asynchronous localization of photoswitching emitters", *Biophysical journal* **93**, 3285.

[75] K. A. Willets, "Probing local electromagnetic field enhancements on the surface of plasmonic nanoparticles", *Progress in Surface Science* **87**, 209. DOI: 10.1016/j.progsurf.2012.08.001.

[76] R. R. Frontiera, A.-I. Henry, N. L. Gruenke, R. P. Van Duyne, "Surface-enhanced femtosecond stimulated raman spectroscopy", *The Journal of Physical Chemistry Letters* **2**, 1199. DOI: 10.1021/jz200498z.

[77] S. Wu, M. T. Sheldon, "Optical power conversion via tunneling of plasmonic hot carriers", *ACS Photonics* **5**, 2516. DOI: 10.1021/acsphotonics.8b00347.

[78] B. S. Hoener, *et al.*, "Plasmonic sensing and control of single-nanoparticle electrochemistry", *Chem* **4**, 1560. DOI: 10.1016/j.chempr.2018.04.009.

[79] A. Naldoni, *et al.*, "Solar-powered plasmon-enhanced heterogeneous catalysis", *Nanophotonics* **5**. DOI: 10.1515/nanoph-2016-0018.

[80] R. Chhabra, *et al.*, "Distance-dependent interactions between gold nanoparticles and fluorescent molecules with DNA as tunable spacers", *Nanotechnology* **20**, 485201.

[81] R. Bardhan, N. K. Grady, J. R. Cole, A. Joshi, N. J. Halas, "Fluorescence enhancement by au nanostructures: Nanoshells and nanorods", *ACS Nano* **3**, 744.

[82] M. Ringler, *et al.*, "Shaping emission spectra of fluorescent molecules with single plasmonic nanoresonators", *Physical Review Letters* **100**, 203002. DOI: 10.1103/PhysRevLett.100.203002.

[83] Z. Zhang, S. J. Kenny, M. Hauser, W. Li, K. Xu, "Ultrahigh-throughput single-molecule spectroscopy and spectrally resolved super-resolution microscopy", *Nature Methods* **12**, 935. DOI: 10.1038/nmeth.3528.

[84] A. Edelstein, N. Amodaj, K. Hoover, R. Vale, N. Stuurman, *Current Protocols in Molecular Biology*, no. SUPPL. 92 (John Wiley & Sons, Inc.).

[85] B. P. Isaacoff, Y. Li, S. A. Lee, J. S. Biteen, "SMALL-LABS: Measuring single-molecule intensity and position in obscuring backgrounds", *Biophysical Journal* **116**, 975. DOI: 10.1016/j.bpj.2019.02.006.

[86] H. J. Goldwyn, K. C. Smith, J. A. Busche, D. J. Masiello, "Mislocalization in plasmon-enhanced single-molecule fluorescence microscopy as a dynamical young's interferometer", *ACS Photonics* **5**, 3141. DOI: 10.1021/acsphotonics.8b00372.

[87] Faraday Michael, "X. the bakerian lecture. —experimental relations of gold (and other metals) to light", *Philosophical Transactions of the Royal Society of London* **147**, 145. DOI: 10.1098/rstl.1857.0011.

[88] M. Das, K. H. Shim, S. S. A. An, D. K. Yi, "Review on gold nanoparticles and their applications", *Toxicology and Environmental Health Sciences* **3**, 193. DOI: 10.1007/s13530-011-0109-y.

[89] Y.-C. Yeh, B. Creran, V. M. Rotello, "Gold nanoparticles: preparation, properties, and applications in bionanotechnology", *Nanoscale* **4**, 1871. DOI: 10.1039/C1NR11188D.

[90] D. Huang, *et al.*, "Photoluminescence of a plasmonic molecule", *ACS Nano* **9**, 7072. DOI: 10.1021/acsnano.5b01634.

[91] J. Mertens, M. E. Kleemann, R. Chikkaraddy, P. Narang, J. J. Baumberg, "How light is emitted by plasmonic metals", *Nano Letters* **17**, 2568. DOI: 10.1021/acs.nanolett.7b00332.

[92] Y.-Y. Cai, *et al.*, "Photoluminescence of gold nanorods: Purcell effect enhanced emission from hot carriers", *ACS Nano* **12**, 976. DOI: 10.1021/acsnano.7b07402.

[93] G. Grover, W. Mohrman, R. Piestun, "Real-time adaptive drift correction for super-resolution localization microscopy", *Optics Express* **23**, 23887. DOI: 10.1364/OE.23.023887.

[94] D. Boyer, P. Tamarat, A. Maali, B. Lounis, M. Orrit, "Photothermal imaging of nanometer-sized metal particles among scatterers", *Science* **297**, 1160. DOI: 10.1126/science.1073765.

[95] A. Gaiduk, M. Yorulmaz, M. Orrit, "Correlated absorption and photoluminescence of single gold nanoparticles", *ChemPhysChem* **12**, 1536. DOI: 10.1002/cphc.201100167.

[96] M. Selmke, M. Braun, F. Cichos, "Photothermal single-particle microscopy: Detection of a nanolens", *ACS Nano* **6**, 2741. DOI: 10.1021/nn300181h.

[97] L. Zou, *et al.*, "Current approaches of photothermal therapy in treating cancer metastasis with nanotherapeutics", *Theranostics* **6**, 762. DOI: 10.7150/thno.14988.

[98] C. Bi, *et al.*, "Realizing a record photothermal conversion efficiency of spiky gold nanoparticles in the second near-infrared window by structure-based rational design", *Chemistry of Materials* **30**, 2709. DOI: 10.1021/acs.chemmater.8b00312.

[99] S. Ebrahimi, Y. Akhlaghi, M. Kompany-Zareh, s. Rinnan, "Nucleic acid based fluorescent nanothermometers", *ACS Nano* **8**, 10372. DOI: 10.1021/nn5036944.

[100] S. W. Chu, *et al.*, "Measurement of a saturated emission of optical radiation from gold nanoparticles: Application to an ultrahigh resolution microscope", *Physical Review Letters* **112**, 017402. DOI: 10.1103/PhysRevLett.112.017402.

[101] A. Carattino, M. Caldarola, M. Orrit, "Gold nanoparticles as absolute nanothermometers", *Nano Letters* **18**, 874. DOI: 10.1021/acs.nanolett.7b04145.

[102] J. Huang, W. Wang, C. J. Murphy, D. G. Cahill, "Resonant secondary light emission from plasmonic au nanostructures at high electron temperatures created by pulsed-laser excitation", *Proceedings of the National Academy of Sciences* **111**, 906. DOI: 10.1073/pnas.1311477111.

[103] S. Moon, *et al.*, "Spectrally resolved, functional super-resolution microscopy reveals nanoscale compositional heterogeneity in live-cell membranes", *Journal of the American Chemical Society* **139**, 10944. DOI: 10.1021/jacs.7b03846.

[104] S. R. Kirchner, *et al.*, "Snapshot hyperspectral imaging (SHI) for revealing irreversible and heterogeneous plasmonic processes", *The Journal of Physical Chemistry C* **122**, 6865. DOI: 10.1021/acs.jpcc.8b01398.

[105] T. Kim, S. Moon, K. Xu, "Information-rich localization microscopy through machine learning", *bioRxiv* DOI: 10.1101/373878.

[106] M. P. M. H. Benoit, H. Sosa, *Single Molecule Analysis: Methods and Protocols*, E. J. G. Peterman, ed., Methods in Molecular Biology (Springer New York), pp. 199–216.